ISPRS Journal of Photogrammetry and Remote Sensing 237 (2026) 94–112

Contents lists available at ScienceDirect

ISPRS Journal of Photogrammetry and Remote Sensing

journal homepage: www.elsevier.com/locate/isprsjprs

Bayesian polarimetric detector for improved forest loss monitoring using dual-polarization Sentinel-1 data

Marta Bottani [a,b,c,d,*], Laurent Ferro-Famil [b,d], Thuy Le Toan [e], Juan Doblas Prieto [e], Stéphane Mermoz [e], Thierry Koleck [c,d]

[a] TéSA, 7 boulevard de la Gare, Toulouse, 31500, France
[b] ISAE-Supaero, 10 Avenue Marc Pélegrin, Toulouse, 31400, France
[c] Centre National d'Etudes Spatiales (CNES), 18 Avenue Edouard Belin, Toulouse, 31400, France
[d] CESBIO, University of Toulouse, CNES/CNRS/INRAE/IRD/UT3, 18 Avenue Edouard Belin, Toulouse, 31400, France
[e] GlobEO, 18 Avenue Edouard Belin, Toulouse, 31400, France

ARTICLE INFO

Keywords:
Deforestation
Change detection
Near real-time
Sentinel-1
Polarimetry
Time series

ABSTRACT

This study investigates the synergistic use of dual-polarization Sentinel-1 time series for forest loss monitoring across mixed land-cover types. While VH polarization generally provides higher contrast between intact vegetation and deforested areas, VV polarization is assumed to be more effective over areas characterized by vegetation remnants left after clearing. These insights motivate the development of *fpol*-BOCD, an unsupervised Bayesian polarimetric change detection method with Near Real-Time (NRT) capabilities. The algorithm is designed to leverage the complementary scattering properties of both polarizations, improving detection sensitivity across diverse land-cover conditions. Notably, *fpol*-BOCD jointly processes VH and VV Sentinel-1 data with comparable computational complexity relative to single-polarization approaches. Evaluation is performed using two datasets of forest loss events, extracted from the MapBiomas Alerta reference dataset for 2020 in the Cerrado and Amazon biomes in Brazil. One dataset focuses on small-scale clearings (0.1–2 hectares), while the other includes a randomly selected subset of larger deforested patches. The method improves detection accuracy by approximately 10% compared to single-polarization BOCD methods in areas likely containing residual vegetation after clearing, e.g., small disturbances in the Cerrado and large ones in the Amazon, while producing very few false alarms relative to the simple merging of single-polarization alerts. Additionally, *fpol*-BOCD outperforms the operational optical-based GLAD-L alerts in the Cerrado, achieving a 47% increase in true detections In the Amazon, a comparison with the operational SAR-based RADD alerts shows a 34% increase in true positives for small clearings. The detection speed of *fpol*-BOCD matches single-polarization BOCD methods. Temporal analysis shows a peak in forest loss during the dry season, with unexpected early wet-season increases likely linked to a lengthening of the dry period. Overall, results highlight the value of polarimetric data for efficient, more accurate forest loss monitoring in complex tropical environments.

1. Introduction

Deforestation is one of the most pressing environmental challenges of our time. Driven by agricultural expansion, logging, infrastructure development, and other anthropogenic pressures, forest loss contributes significantly to environmental degradation (FAO, 2020). Tropical forests, in particular, are experiencing rapid transformation, underscoring the urgent need for effective monitoring systems that can inform conservation policies and land management decisions. While optical remote sensing has been widely used for forest monitoring (Hansen et al., 2013, 2016), its performance is limited in persistently cloudy regions (Verbesselt et al., 2012). In contrast, Synthetic Aperture Radar (SAR) systems operate independently of cloud cover, providing consistent and frequent observations that make SAR-based approaches increasingly valuable for NRT forest loss detection (Reiche et al., 2016).

Concerning SAR-based methods, polarimetric diversity in PolSAR data enhances sensitivity to vegetation structure and moisture by capturing how targets scatter radar signals under different polarizations (Durden et al., 1989; Van Zyl, 1989; Neumann et al., 2010; Arii et al., 2010; Papathanassiou et al., 2021). While forest analysis using PolSAR has traditionally been conducted with longer wavelengths (L-

* Corresponding author at: ISAE-Supaero, 10 Avenue Marc Pélegrin, Toulouse, 31400, France.
E-mail address: marta.bottani@isae-supaero.fr (M. Bottani).

https://doi.org/10.1016/j.isprsjprs.2026.04.028
Received 7 October 2025; Received in revised form 10 April 2026; Accepted 13 April 2026
Available online 22 April 2026
0924-2716/

or P-band) (Ferro-Famil et al., 2001; Papathanassiou et al., 2021) to reduce the impact of volume scattering saturation (Le Toan, 2014), the launch of missions such as Sentinel-1 — with its globally available dual-polarization C-band data — has opened new opportunities for operational, large-scale monitoring. At C-band, polarimetric data have been successfully used for estimating plant structure (Furtado et al., 2016), moisture content (Bourgeau-Chavez et al., 2013; El-Hajj et al., 2017; Magagi et al., 2022), and biomass (Persson et al., 2022), thereby facilitating enhanced analyses of forest dynamics (Hoekman et al., 2020), crop health assessment (Jiao et al., 2011; Veloso et al., 2017), and crop classification (Skriver, 2012; Lopez-Sanchez et al., 2014)

Timely forest loss detection requires high revisit frequency, data continuity, and broad spatial coverage, ideally from freely accessible sources. Sentinel-1 meets these requirements with its six-day revisit time over the tropics, enabled by its two-satellite constellation, and its open-access policy. As a result, it has become a valuable asset for NRT forest loss monitoring, with most existing approaches making use of a single polarimetric channel (Bouvet et al., 2018; Reiche et al., 2018a,b; Doblas et al., 2020; Mermoz et al., 2021; Ballère et al., 2021; Bottani et al., 2025a). While some studies acknowledge the importance of leveraging both polarizations (Hoekman et al., 2020; Mullissa et al., 2024), they often process each channel independently and combine the outputs during post-processing. This approach falls short of exploiting the full potential of the data and rarely articulates the specific contributions of each channel. A critical gap remains in the literature regarding both the potential of dual-polarimetric C-band SAR data to enhance detection capabilities and the development of methods for jointly processing these channels to improve forest loss monitoring.

This paper aims first to explore the potential advantages of jointly employing dual-polarimetric Sentinel-1 data for detecting forest loss over various land covers. By leveraging the distinct sensitivities of the VH and VV polarimetric channels previously investigated in Bottani et al. (2025b), forest loss detection accuracy and reliability are expected to be enhanced. Secondly, building on the methodology proposed in Bottani et al. (2025a), a Bayesian polarimetric detector, denoted as $fpol$-BOCD, is developed for NRT monitoring of forest loss. The results produced by $fpol$-BOCD are validated against reference data from the Cerrado and Amazon biomes in Brazil and compared with single-polarization detectors and operational methods to assess performance improvements.

1.1. Forest monitoring using C-band PolSAR data

Radar polarimetry is an important tool for characterizing imaged objects and media by decomposing complex wave–matter interactions into distinct scattering mechanisms (Huynen, 1970; Van Zyl, 1989; Durden et al., 1989; Cloude and Pottier, 1996; Van Zyl and Kim, 2011). Radar backscatter is shaped by the interaction between the transmitted signal and the target, which results in a combination of scattering mechanisms — such as surface scattering, double-bounce reflection, and volume scattering — whose relative importance depends on several factors, including geometry, target structure, dielectric properties, and acquisition parameters such as frequency, polarization, and incidence angle (Van Zyl, 1989; Lee and Pottier, 2009; Ferro-Famil and Pottier, 2014; Abdo et al., 2021).

Unlike fully polarimetric radar systems, which exploit polarization diversity for both transmission and reception, dual-polarization radars transmit in a single polarization and receive two orthogonal polarization components. Most spaceborne systems operate in the horizontal (H) and vertical (V) polarization basis. Sentinel-1 is a dual-polarization system that acquires the VV and VH scattering coefficients, S_{VV} and S_{VH}. In this configuration, co- and cross-polarized echoes are known to be uncorrelated over natural environments with mild topography (Nghiem et al., 1992), and the available second-order polarimetric information reduces to a pair of reflectivity estimates, I_{VV} and I_{VH} (Cloude and Pottier, 1997; Freeman and Durden, 1998).

In dense tropical forests, the C-band signal primarily interacts with the canopy's upper layers (Imhoff, 1995), where single scattering from leaves and small twigs dominates the co-polarized (HH, VV) response through first-order volume scattering (Karam et al., 1992). In the cross-polarized channels (HV or VH), multiple scattering within the canopy leads to a generally lower, but also stable, response that reflects the mature forest structure (Picard et al., 2004). Mature forests and secondary growth vegetation may exhibit similar responses at C-band due to backscatter saturation (Rosenqvist and Killough, 2018). Post-logging, both co- and cross-polarized signals show significant temporal variations from changes in soil moisture, debris, or surface roughness, often masking the effects of forest regrowth (Hoekman and Quiñones, 2000). Cross-polarized SAR images generally provide clearer differentiation between forested and non-forested areas, reducing the ambiguities seen in co-polarized images, except in cases where residual vegetation is left after clearing, which can saturate the cross-polarization signal (Picard et al., 2004). In sparsely vegetated regions, signal penetration through the canopy increases, revealing double-bounce effects in co-polarized backscatter. Ground scattering dominates where vegetation is minimal, while volume scattering and vegetation–ground interactions become more pronounced with increasing biomass (Picard et al., 2004; Rosenqvist and Killough, 2018).

1.2. Polarimetric handling in timely forest loss monitoring

Several NRT forest loss monitoring methods using Sentinel-1 imagery have been developed in recent years and are now operational. These methods either rely on scalar backscatter measurements derived from a single polarization channel or use measurements from both channels, treated separately and combined during post-processing to generate deforestation alerts.

1.2.1. Single-polarization approaches

The method in Reiche et al. (2018b) analyzes the temporal relationship between fires and forest-cover loss in tropical regions by combining Sentinel-1 NRT forest loss information with VIIRS active fire alerts. Cross-polarized Sentinel-1 data are found to be more effective than co-polarized data for detecting forest-cover loss because of higher sensitivity to structural changes, with VH reflectivity consistently outperforming VV in both timeliness and accuracy. A multi-sensor NRT deforestation detection method is proposed in Reiche et al. (2018a), combining Sentinel-1 C-band SAR, ALOS-2 PALSAR-2 L-band SAR, and Landsat optical time series. The approach uses a probabilistic model to detect deforestation in tropical dry forests. In this context, Sentinel-1 VV time series are employed due to the limited availability of VH data for the study region and period.

A forest loss detection method based on geometric shadow artifacts along deforested edges and patch reconstruction is proposed in Bouvet et al. (2018). In the Peruvian study area, VH and VV time series show comparable performance, and VV polarization is selected, while acknowledging that both channels can be effective under certain conditions. In contrast, the evaluation reported in Doblas et al. (2020), which compares two deforestation detection techniques — adaptive linear thresholding and maximum likelihood classification — using Sentinel-1 A data, demonstrates that VH reflectivity provides clearer results for detecting changes following deforestation, whereas VV reflectivity often introduces more false alarms. Further evidence in Mermoz et al. (2021) indicates that VH data provide slightly better separability between forest loss and intact forest, especially in challenging environments like hilly terrain. In contrast, in flatter regions, both VH and VV polarimetric channels show comparable performance.

1.2.2. Dual-polarization post-processing fusion approaches

A method for NRT monitoring of tropical forest changes combines time-series analysis of small disturbances and linear features to detect deforestation in regions such as the Amazon and Borneo (Hoekman et al., 2020). This approach highlights the importance of concurrent decreases in both VV and VH reflectivities for reliable detection, noting that a decline in only one channel is insufficient for robust decisions.

The algorithm generating the RADD deforestation alerts (Reiche et al., 2021) processes VV and VH polarization time series separately and combines the outputs using a comparative rule that selects the higher non-forest probability. A SAR-based deep learning approach for forest disturbance detection in tropical dry forests is proposed in Mullissa et al. (2023), utilizing dual-polarization Sentinel-1 data. Separate deep neural network models are trained on VV and VH polarizations for different regions, and disturbance probabilities from both polarimetric channels are later combined to improve detection. The LUCA dataset introduced in Mullissa et al. (2024) uses Sentinel-1 VH and VV data with machine learning techniques to monitor global forest changes. The authors state that for an alert to be considered reliable, it must be detected in both polarization channels, which can lead to omission errors.

Despite the extensive literature on the use of Sentinel-1 data for forest loss monitoring, the preference for one polarimetric channel over the other remains ambiguous. Various studies report conflicting results regarding the effectiveness of VH versus VV polarizations in detecting forest change, yet many do not provide a comprehensive explanation for their findings. Furthermore, works that consider both polarimetric channels often merge the results from separate analysis, rather than processing the joint information, which results in omissions if a change is expected on both channels (Hoekman et al., 2020), or false alarms if a change is flagged based on just one polarization (Ygorra et al., 2021). These discrepancies highlight a gap in understanding the underlying mechanisms that influence the performance of Sentinel-1 polarization channels in different environmental contexts. Therefore, the following sections investigate the conditions under which each polarization channel may be more advantageous for timely forest loss detection.

2. Study region and reference data

2.1. The Cerrado

The Cerrado is one of the world's most biologically diverse tropical savannas, covering around 2 million square kilometers in eastern Brazil. As Brazil's second-largest biome after the Amazon, the Cerrado occupies about 21% of the country's total land area. The landscape of the Cerrado is primarily characterized by savanna formations, which roughly represent 73% of the biome's land cover, interspersed with forests covering approximately 19% and grasslands accounting for about 8% (Azevedo et al., 2021). The Cerrado experiences a semi-humid tropical climate, with average annual precipitation levels between 80 and 200 cm (Ratter et al., 1997). The region undergoes two distinct seasons: a dry period, typically from April to September, and a rainy period, lasting from October to March. Seasonal growth during the rainy season and drying during the dry season lead to periodic vegetation changes, which in turn cause fluctuations in SAR backscatter.

Recently, the Cerrado has become a major hotspot for deforestation (Miranda et al., 2019). Approximately 75% of the biome's area is privately owned, intensifying pressures on land for agriculture, cattle ranching, and other economic activities. These factors have contributed to the widespread conversion of native vegetation into agricultural land, making the Cerrado the second-most deforested biome in Brazil after the Amazon (RAD2023, 2024). Recent deforestation trends in the Cerrado show alarming habitat loss, with 432,000 hectares of native vegetation cleared in 2020 alone (Azevedo et al., 2021; RAD2023, 2024). Deforestation rates peak during the dry season, when the lack of rainfall facilitates land clearing activities.

A significant portion of the deforestation in the Cerrado is driven by the expansion of large-scale soy plantations (Rausch et al., 2019). These industrial operations often involve the clearing of extensive land parcels, and are characterized by systematic and efficient land-clearing practices that result in uniformly bare soil surfaces that simplify remote sensing-based detection (De Andrade Aragão et al., 2022). In contrast, smaller-scale clearings have increasingly emerged since the early 2000s (Pinheiro et al., 2024). These are commonly associated with subsistence or smallholder agriculture, characterized by less systematic clearing practices, resulting in residual vegetation and rougher textures that complicate detection (Rasmussen et al., 2016). To the best of the authors' knowledge, operational forest loss monitoring in the Cerrado is limited due to seasonality-dependent variability affecting backscattered signals. While LUCA (Mullissa et al., 2024) provides operational SAR-based alerts over the Cerrado, the dataset is not freely accessible, leaving existing monitoring efforts primarily reliant on optical technologies, which are significantly hindered by persistent cloud cover.

2.2. The Brazilian Amazon

The Brazilian Amazon, i.e., *Amazonia*, covers roughly 5 million square kilometers and is predominantly composed of moist broadleaf tropical rainforest vegetation (Shimabukuro et al., 2016). The dry season typically lasts from May to September, and the rainy season from October to April, although their onset and end vary with latitude. Annual rainfall averages 225 cm, varying from 150 cm in the drier north and south to 300 cm in the wetter northwest.

Forest loss in the Amazon has been a major concern, especially over the past five decades, with nearly 90% of deforestation for pasture and agriculture occurring between 1970 and 1988. This trend followed the relocation of Brazil's capital to Brasília and the construction of major roads (Nunes et al., 2014; Veríssimo et al., 1992). Government agencies supported this development through fiscal incentives and subsidized credit, which largely benefited large landowners. These actors cleared extensive forest areas, often as speculative investments rather than for productive use (Acker, 2021). Beyond agricultural and pasture expansion, a marked shift in deforestation dynamics has been observed in recent years. While the occurrence of large clearings has declined, the number of small patches has increased dramatically (Kalamandeen et al., 2018). Small-scale practices contribute to forest degradation by opening access roads and disrupting forest structure, thereby increasing vulnerability to fire and further clearing (Asner et al., 2005). In 2020 alone, 843,000 hectares of forest formations were cleared in the Amazon (RAD2023, 2024).

2.3. Forest definition

In the present work, forest formations are defined based on the MapBiomas Alerta classification criterion (RAD2023, 2024).

Cerrado. Forests are areas with a continuous canopy height exceeding 7 m. This category includes riparian forests, gallery forests, dry forests, and forested savannas. In contrast, savanna formations are characterized by a heterogeneous structure composed of trees, shrubs, and herbaceous layers, with canopy heights ranging from 3 to 6 m. According to MapBiomas Alerta, forest loss refers to the complete removal of native vegetation, explicitly excluding selective logging or degradation that does not result in full canopy loss. This study adopts a broad definition of deforestation that encompasses all forms of native vegetation suppression, including those occurring in savanna-like areas.

Amazonia. Forests are characterized by dense, continuous canopies exceeding 7 m in height. This definition includes evergreen, semi-deciduous, and deciduous non-flooded vegetation types. Forest loss is also defined as the complete removal of native vegetation.

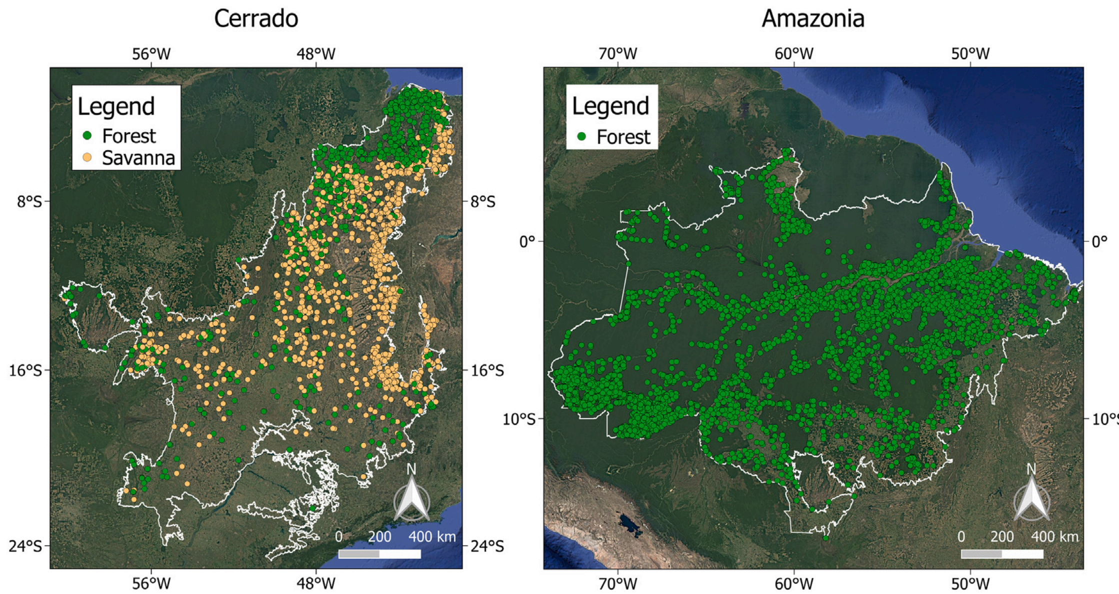

Fig. 1. Spatial distribution of MapBiomas Alerta reference polygons across the Cerrado and Amazon biomes in 2020, highlighting the original land cover prior to deforestation. Optical background image from Google Earth (©2025 Google).

2.4. Reference data

The choice of the study area is supported by the availability of reliable reference data from MapBiomas Alerta (RAD2023, 2024), an initiative that compiles deforestation alerts from various operational remote sensing-based detection systems in Brazil. These polygon-based alerts are aggregated, validated, and refined using high-resolution satellite imagery (PlanetScope, with a 3.7 m spatial resolution) to delineate deforested areas. This work focuses on deforestation monitoring for the year 2020, which corresponds to the final year of full operational capacity for Sentinel-1B, resulting in an input dataset with a 6-day revisit time.

The proposed algorithm is applied in a rectangular buffer region surrounding each reference polygon, averaging 2.6 times the polygon's area. Forest loss is assessed at the polygon scale. A detection is triggered if a significant portion of a polygon is identified as forest loss by the proposed method; that is, a polygon is classified as forest loss if:

$$\frac{A_{\text{detected}}}{A_{\text{polygon}}} \geq T_{\text{poly}}, \tag{1}$$

where A_{detected} is the area within the polygon where forest loss is detected, A_{polygon} is the total area of the polygon, and T_{poly} is a threshold. True positives represent polygons classified as forest loss by both the proposed method and MapBiomas Alerta for 2020. In contrast, false negatives correspond to polygons marked as forest loss by MapBiomas Alerta but missed by the proposed method during the same period.

To account for potential bias caused by undetected disturbed areas in the MapBiomas Alerta dataset, false positives are estimated using a temporal approach. Specifically, MapBiomas Alerta polygons are marked as disturbed based on the assumption of prior land cover (e.g., forest or savanna). Once marked, they are masked out for subsequent years. Therefore, MapBiomas Alerta polygons from 2021 are analyzed to identify false positives which are defined as a forest loss detected by the proposed method in 2020 but recorded by MapBiomas Alerta as occurring in 2021.

Two reference datasets, extracted from MapBiomas Alerta polygons collected over the Cerrado and Amazon biomes (accessed at: https://alerta.mapbiomas.org/), are defined. The first reference dataset includes all small-scale deforestation polygons, with areas ranging from 0.1 to 2 hectares, collected by MapBiomas Alerta over the Cerrado. These polygons have a mean size of $\mu_{size} = 0.993$ ha and a standard deviation of $\sigma_{size} = 0.329$ ha. In the Amazon, all polygons between 0.1 and 1 hectare are included, while 3000 polygons sized between 1 and 2 hectares are randomly sampled to manage computational effort. These polygons have a mean size of $\mu_{size} = 1.099$ ha and a standard deviation of $\sigma_{size} = 0.249$ ha. To further maintain a manageable computational burden, the second reference dataset is constructed using stratified sampling (Robb and Cochran, 1963), applied to the MapBiomas Alerta polygons according to three predefined size categories: 2–6 hectares, 6–20 hectares, and greater than 20 hectares. Throughout the monitoring period, most of the reference areas were converted into agricultural land, with the rate and extent of deforestation influenced by factors such as geographical location within the biome and local meteorological conditions. The number of reference polygons per size class are provided in Table 1, while Fig. 1 illustrates the spatial distribution of the reference polygons, which cover 8000 hectares in the Cerrado and 13,400 hectares in the Amazon, highlighting the original land cover prior to deforestation.

3. Motivation

3.1. Synergistic analysis of co- and cross-polarized channels

This section explores the backscatter statistics of co-polarized (VV) and cross-polarized (VH) Sentinel-1 channels in the reference datasets presented earlier for different vegetation types, polarizations, and forest conditions. Specifically, Sentinel-1 data consist of Radiometrically Terrain-Corrected (RTC) calibrated intensity (γ^0) time series, converted to a logarithmic scale as $\zeta^0 = \log(\gamma^0)$, where for each pixel a single acquisition geometry (ascending or descending) is selected to avoid pseudo-changes in backscatter arising from mixed-orbit effects. It is worth noting that no speckle filtering is applied in the pre-processing of the original 10-meter pixel spacing, multi-looked products, in order to preserve the finest resolution achievable for loss detection using Sentinel-1 RTC data, that is 20 m in ground range and 22 m in azimuth. This decision aims at enhancing the effectiveness of the method in detecting small-scale forest loss (Bottani et al., 2025a).

The temporal statistical behavior of backscatter over intact vegetation is characterized using co- and cross-polarized Sentinel-1 data from 01/01/2017 to 31/12/2019, resulting in 86 acquisitions, while the backscatter response to forest loss is represented by the values of three consecutive acquisitions immediately following the deforestation

Table 1
Number of reference polygons by clearing size class. A_i: class of polygon's size. F: Forest, S: Savanna.

2020 Reference Dataset					
		Small Clearings	Large Clearings		
Size		$0.1 \leq A_0 < 2$ ha	$2 \leq A_1 < 6$ ha	$6 \leq A_2 < 20$ ha	$A_3 \geq 20$ ha
Amazonia		6,590	264	173	63
Cerrado		1,970	189	179	132
	F	887	70	64	58
	S	1,083	111	103	94
2021 Reference Dataset					
Amazonia		2,657	110	94	46
Cerrado		415	134	94	72
	F	137	61	44	31
	S	278	73	50	41

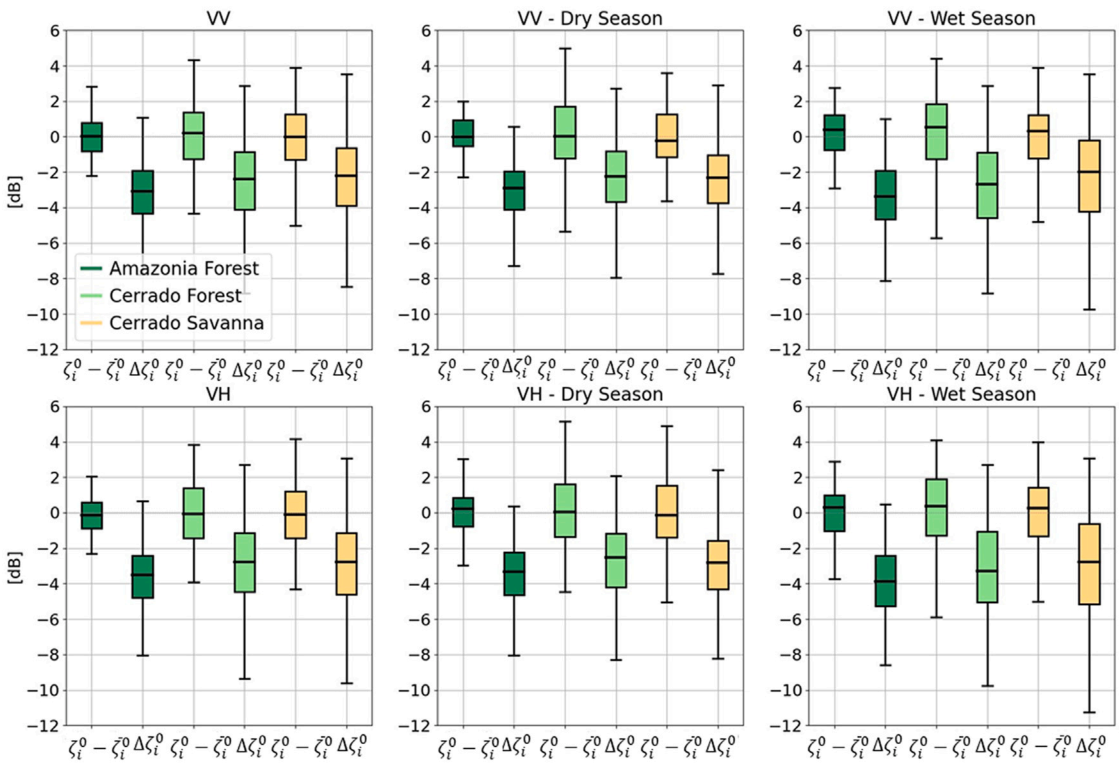

Fig. 2. Boxplots illustrating intact vegetation backscatter relative to the mean ($\zeta_i^0 - \overline{\zeta}_i^0$) and deforestation-induced drops ($\Delta\zeta_i^0$), grouped by polarization, land cover, and season. Each box shows the median (central line), interquartile range (box), and non-outlier range (whiskers: 1.5 × interquartile range).

date reported in MapBiomas Alerta, i.e., t_{MBA}. For both cases, the computation follows:

$$\overline{\zeta}_i^0 = \frac{1}{N_{\mathcal{P}_i}} \sum_{p \in \mathcal{P}_i} \frac{1}{N_{\mathcal{T}_i}} \sum_{t \in \mathcal{T}_i} \zeta_{i,p,t}^0, \tag{2}$$

where $N_{\mathcal{P}_i}$ is the number of pixels in polygon $\mathcal{P}_i$, and $N_{\mathcal{T}_i}$ is the number of acquisitions of interest within the time window $\mathcal{T}_i$, defined for the two cases as follows:

$$\overline{\zeta}_i^0 = \begin{cases} \overline{\zeta}_{i,\text{intact}}^0 & \mathcal{T}_i : \{01/01/2017 \leq t \leq 31/12/2019\} \\ \overline{\zeta}_{i,\text{deforestation}}^0 & \mathcal{T}_i : \{t_{\text{MBA}} \leq t < t_{\text{MBA}} + 3\}. \end{cases} \tag{3}$$

The backscatter drop associated with forest loss for each polygon is given by:

$$\Delta\zeta_i^0 = \overline{\zeta}_{i,\text{intact}}^0 - \overline{\zeta}_{i,\text{deforestation}}^0. \tag{4}$$

Fig. 2 shows boxplots for intact vegetation, $\zeta_i^0 - \overline{\zeta}_i^0$, and backscatter drops, $\Delta\zeta_i^0$, following deforestation. The results are differentiated by biome, polarimetric channel, land cover type, and season to assess possible seasonal variations.

Preliminary observations suggest that the backscatter of intact vegetation exhibit lower variability, i.e., lower standard deviation, compared to those of deforested areas. This difference can be attributed to the heterogeneous nature of cleared land, including the presence of exposed soil or agricultural activities. The VH channel demonstrates a more pronounced response to vegetation loss, likely due to its higher sensitivity to volume scattering. This trend is observed consistently across seasons and land cover types.

Forests. In the Amazon, intact forests exhibit 1.8 times lower signal variability than those in the Cerrado. Moreover, deforestation results in a backscatter drop 1.3 times greater in the Amazon, while post-clearing variability is approximately 9% lower than in the Cerrado. Within forests in the Cerrado, the mean backscatter drop following deforestation is 1.2 times larger compared to savannas over both VH and VV channels. Differentiating the analysis by dry and wet seasons does not provide new insights, aside from a tendency toward increased

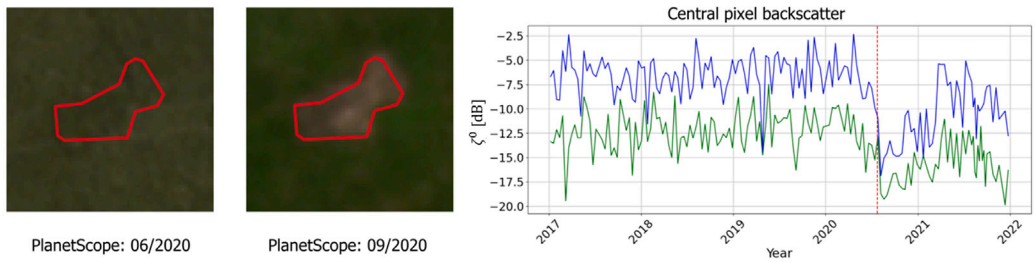

(a) Example 1. Central pixel location: (47.78327°W, 7.68962°S), original cover: savanna, date of clearing: 15/07/2020.

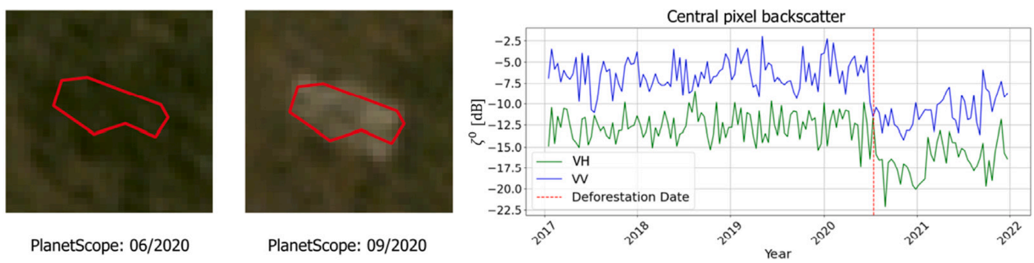

(b) Example 2. Central pixel location: (43.30150°W, 2.87119°S), original cover: forest, date of clearing: 24/07/2020.

Fig. 3. Examples of VV-polarization potential in detecting forest loss.

variability during the wet season compared to the dry season. Additionally, backscatter drops tend to be larger during the dry season than the wet season for the VV channel.

Savannas. In intact savanna regions, backscatter is more variable than in forests. The mean backscatter drop observed in savannas after deforestation is generally lower than that seen in forests. Nonetheless, during the dry season the backscatter drop variability tends to be slightly lower than in forests in the Cerrado. In contrast, the variability of the drop increases during the wet season, surpassing that of the forest class.

The results shown in Fig. 2 clearly show pronounced overlaps in reflectivity levels between intact vegetation and deforested areas, regardless of land cover type, season, or polarization channel. This observation suggests that thresholding, as commonly used in existing forest loss monitoring methods (Bouvet et al., 2018; Mermoz et al., 2021; Ballère et al., 2021; Doblas et al., 2022; Carstairs et al., 2022), may prove insufficient for effectively identifying changes in mixed-land cover areas, emphasizing the need to develop a processing approach centered on time series analysis for reliable detection.

Considering polarization-specific results, VH polarization shows a larger mean backscatter difference between intact and deforested areas across both land cover types and in both biomes, making it potentially more effective for distinguishing changes. However, due to its sensitivity to volume scattering, VH might face challenges in detecting disturbed areas where some vegetation remnants stay on the ground after deforestation. Conversely, VV polarization generally displays a smaller mean backscatter difference between intact and deforested areas, which may reduce its effectiveness in distinguishing deforestation events. Nevertheless, VV might perform better than VH in detecting deforestation when significant debris remains on the ground after clearing, enabling more effective and rapid disturbance detection.

Fig. 3 shows two examples of polygons extracted from the reference dataset, for which VV polarization appears more suitable than VH for detecting deforestation. The polygon in Fig. 3(a) is characterized by $\Delta\zeta^0_{VV} = 5.2$ dB and $\Delta\zeta^0_{VH} = 4.7$ dB, whereas the polygon in Fig. 3(b) has $\Delta\zeta^0_{VV} = 7.8$ dB and $\Delta\zeta^0_{VH} = 5.0$ dB. Both examples support the suitability of VV polarization for detecting deforestation in some cases and highlight the value of combining both polarimetric channels to improve performance.

4. Methods

4.1. Bayesian polarimetric detector

This section presents a novel polarimetric detector for NRT forest loss monitoring, building on the Bayesian Online Changepoint Detection (BOCD) method developed in Bottani et al. (2025a) and extending it to process polarimetric time series.

4.1.1. Generic polarimetric BOCD

Consider $\mathbf{X}_{1:t} = (\mathbf{x}_1, \dots, \mathbf{x}_t) \in \mathbb{R}^{2\times t}$, where each $\mathbf{x}_i = (x_{1,i}, x_{2,i})^T \in \mathbb{R}^2$ is a vector containing the log-scale dual-polarization reflectivity measurements, $x_1 = \zeta^0_{VH}$ and $x_2 = \zeta^0_{VV}$, at time i.

Online Bayesian changepoint detection relies on modeling the number of acquisitions elapsed since the last changepoint, referred to as the run length (Adams and MacKay, 2007), and denoted r_t at time t. At each newly observed datum, the run length either resets to 0 if a change is detected, or increments to $r_{t-1}+1$ otherwise, as depicted in Fig. 4. The objective is to detect changes using the Maximum *A Posteriori* (MAP) estimate of the run length. This requires estimating the posterior distribution of the run length:

$$p(r_t|\mathbf{X}_{1:t}) = \frac{p(r_t, \mathbf{X}_{1:t})}{\sum_{r_t=0}^{t} p(r_t, \mathbf{X}_{1:t})}, \tag{5}$$

which is proportional to the joint distribution of the run length and the data observed up to time t (Bottani et al., 2025a):

$$p(r_t, \mathbf{X}_{1:t}) = \sum_{r_{t-1}=0}^{t-1} p\left(\mathbf{x}_t|\mathbf{r}_{t-1:t}, \mathbf{X}_{t-1}^{(r_{t-1})}\right) p(r_t|r_{t-1}) p(r_{t-1}, \mathbf{X}_{1:t-1}), \tag{6}$$

with $\mathbf{r}_{t-1:t} = (r_{t-1}, r_t)^T$, and:

$$p\left(\mathbf{x}_t|\mathbf{r}_{t-1:t}, \mathbf{X}_{t-1}^{(r_{t-1})}\right) = \begin{cases} 0 & \text{if } r_{t-1} \neq r_t - 1 \text{ and } r_t > 0 \\ p\left(\mathbf{x}_t \left| \mathbf{X}_{t-1}^{(r_{t-1})}\right.\right) & \text{otherwise.} \end{cases} \tag{7}$$

In (6), the term $p(r_{t-1}, \mathbf{X}_{1:t-1})$ represents the information carried over from the previous time step, while $p(r_t|r_{t-1})$ denotes the probability of transition (Bottani et al., 2025a). The posterior predictive $p(\mathbf{x}_t|\mathbf{r}_{t-1:t},$

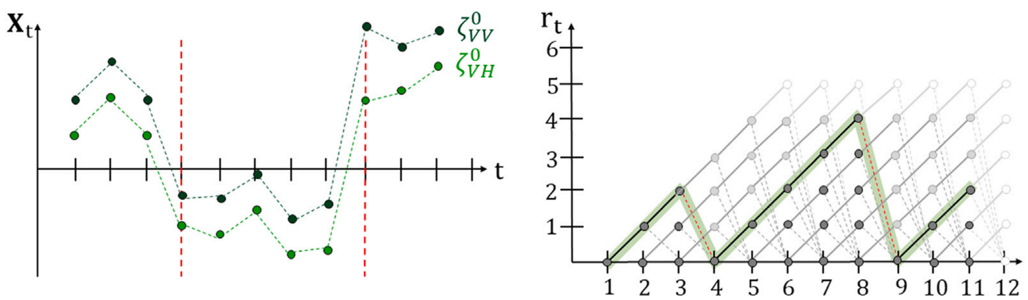

Fig. 4. Dual-polarization backscatter time series with changes highlighted by red dashed lines (left). Corresponding r_t map (right).

$\mathbf{X}_{t-1}^{(r_{t-1})}$) in (7), with $\mathbf{X}_{t-1}^{(r_{t-1})} = (\mathbf{x}_{t-1-r_{t-1}}, \dots, \mathbf{x}_{t-1})^T$, provides the distribution of the next observation given the data observed up to that point, and for the segment $\mathbf{r}_{t-1}$. The data samples acquired between two consecutive changepoints, i.e., belonging to a segment as shown in Fig. 4, are assumed to be independent and identically distributed (i.i.d.), with a likelihood distribution $p_\theta(\mathbf{x}_t)$. The posterior predictive distribution can be expressed as:

$$p\left(\mathbf{x}_t|\mathbf{X}_{t-1}^{(r_{t-1})}\right) = \int p(\mathbf{x}_t\,|\theta)\,\pi_{\eta_0}\left(\theta\left|\mathbf{X}_{t-1}^{(r_{t-1})}\right.\right)d\theta, \tag{8}$$

with $\pi_{\eta_0}(\theta)$ representing the prior distribution governing the parameter vector θ. The posterior distribution of the parameters is given by:

$$\pi_{\eta_0}\left(\theta\left|\mathbf{X}_{t-1}^{(r_{t-1})}\right.\right) = \frac{p\left(\mathbf{X}_{t-1}^{(r_{t-1})}\,|\theta\right)\pi_{\eta_0}(\theta)}{\int p\left(\mathbf{X}_{t-1}^{(r_{t-1})}\,|\theta\right)\pi_{\eta_0}(\theta)d\theta}. \tag{9}$$

To avoid the computational cost of evaluating the summation in (9), conjugate priors are employed to replace it with a simple parameter update.

As previously shown, individual Sentinel-1 RTC log-intensity polarimetric channels are Gaussian-distributed (Bottani et al., 2025a). Hence, the polarimetric log-intensity vector $\mathbf{x}_i$ follows a bivariate normal distribution, i.e., $\mathbf{x}_i \sim \mathcal{N}(\boldsymbol{\mu}_i, \boldsymbol{\Sigma}_i)$, with unknown mean and covariance matrix. In this case, the conjugate priors — a normal distribution for the mean vector and an inverse-Wishart distribution for the covariance matrix (Fink, 1997) — yield a normal inverse-Wishart distribution, i.e., $\theta = [\boldsymbol{\mu}, \boldsymbol{\Sigma}] \sim \mathcal{NIW}(\theta; \boldsymbol{\eta}_0)$. The posterior distribution of the parameters follows the same law:

$$p(\boldsymbol{\mu}, \boldsymbol{\Sigma}|\mathbf{X}_m) = \mathcal{N}(\boldsymbol{\mu}|\boldsymbol{\mu}_m, \boldsymbol{\Sigma}/\kappa_m)\,\mathcal{IW}_{\alpha_m}(\boldsymbol{\Sigma}|\mathbf{T}_m), \tag{10}$$

with $\mathbf{X}_m = (\mathbf{x}_0, \dots, \mathbf{x}_m)$ and $\boldsymbol{\eta}(m) = (\boldsymbol{\mu}_m, \alpha_m, \kappa_m, \mathbf{T}_m)$ updated as follows:

$$\begin{aligned} \boldsymbol{\mu}_m &= \frac{\kappa_0\boldsymbol{\mu}_0 + m\bar{\mathbf{x}}}{\kappa_0 + m} \\ \alpha_m &= \alpha_0 + m \\ \kappa_m &= \kappa_0 + m \\ \mathbf{T}_m &= \mathbf{T}_0 + \mathbf{S} + \frac{\kappa_0 m}{\kappa_0 + m}(\bar{\mathbf{x}} - \boldsymbol{\mu}_0)(\bar{\mathbf{x}} - \boldsymbol{\mu}_0)^T. \end{aligned} \tag{11}$$

In (11), the parameters include the mean vector $\boldsymbol{\mu}$, the degrees of freedom α, the shape parameter κ, and the inverse scale matrix $\mathbf{T}$, $\mathbf{S} = \sum_{i=0}^m (\mathbf{x}_i - \bar{\mathbf{x}})(\mathbf{x}_i - \bar{\mathbf{x}})^T$, $\bar{\mathbf{x}} = \frac{1}{m+1}\sum_{i=0}^m \mathbf{x}_i$, and $\boldsymbol{\eta}(0) = \boldsymbol{\eta}_0$. The posterior predictive distribution is known to be a bivariate t-distribution (Murphy, 2007):

$$p(\mathbf{x} \mid \mathbf{X}_m) = t_{2\alpha_m}\left(\mathbf{x}\left|\,\boldsymbol{\mu}_m, \frac{\mathbf{T}_m(\kappa_m+1)}{\alpha_m\kappa_m}\right.\right). \tag{12}$$

This generic version of the polarimetric BOCD is referred to as *gpol*-BOCD.

4.1.2. Sentinel-1 correlation properties over forested areas

The polarimetric response of natural environments, such as forests, is known to exhibit polarimetric symmetry properties, characterized by uncorrelated co- and cross-polarization channels (Nghiem et al., 1992). To evaluate the validity of this assumption, the correlation $|\hat{\rho}|_{VH,VV}$ between Sentinel-1 ζ^0_{VH} and ζ^0_{VV} is estimated over various undisturbed regions in the Cerrado biome. The computation is performed as follows:

$$|\hat{\rho}|_{VH,VV} = \frac{|\langle x_{1_c} x_{2_c}\rangle|}{\sqrt{\langle x_{1_c} x_{1_c}\rangle\langle x_{2_c} x_{2_c}\rangle}}, \tag{13}$$

where $\langle\cdot\rangle$ denotes a boxcar filter of size $N \times N$, and x_{i_c} (with $i = 1, 2$) represents the locally centered value of x_i. Fig. 5 shows ζ^0_{VV} over three 1000×3000-pixel areas, along with the absolute correlation estimated using a boxcar filter of size $N = 11$, confirming the hypothesized polarimetric reflection symmetry. The white dots visible on the correlation plots (right side of Fig. 5) indicate non-stationary areas.

4.1.3. Accounting for polarimetric reflection symmetry

Empirical estimates of the inverse scale matrix $\mathbf{T}_m$, such as those used in (11), tend to converge slowly toward a diagonal form (Joughin et al., 1994). While this bias diminishes asymptotically with an increasing number of independent samples (Touzi et al., 1999), it can lead to the overestimation of low correlation values. Such overestimation, in turn, may impair the change detection process by artificially reducing the rank of the estimated covariance matrix, thereby disrupting its intrinsic structure. This phenomenon likely influences the decisions associated with low r_t values, where only a limited number of samples are available.

To reflect the decorrelation of VV and VH channels over forested environments, two approaches can be adopted.

Adapted generic BOCD. An ad hoc, milder solution is to enforce decorrelation by retaining only the diagonal components of the inverse scale matrix estimate in (10):

$$\mathbf{T}_m \to \widetilde{\mathbf{T}}_m = \mathbf{T}_m \odot \mathbf{I}_M, \tag{14}$$

where $\mathbf{I}_M$ is the identity matrix of size $M \times M$ and $\odot$ represents the element-wise Hadamard product. This version of the polarimetric BOCD is called *dpol*-BOCD, indicating BOCD with a diagonal inverse scale matrix prior.

In this case of normal likelihood and a normal-inverse Wishart prior, the posterior predictive distribution in (8) can be written as:

$$\begin{aligned} p\left(\mathbf{x}_t\left|\mathbf{X}_{t-1}^{(r_{t-1})}\right.\right) = \int &\mathcal{N}(\mathbf{x}_t|\boldsymbol{\mu}, \boldsymbol{\Sigma})\,\mathcal{N}(\boldsymbol{\mu}|\boldsymbol{\mu}_{r_t-1}, \boldsymbol{\Sigma}/\kappa_{r_t-1}) \\ &\mathcal{IW}(\boldsymbol{\Sigma}|\widetilde{\mathbf{T}}_{r_t-1}, \alpha_{r_t-1})\,d\boldsymbol{\mu}\,d\boldsymbol{\Sigma}. \end{aligned} \tag{15}$$

The computation of the summation in (15) over the space of positive definite matrices involves arbitrary covariance matrices $\boldsymbol{\Sigma}$, even when the matrix $\widetilde{\mathbf{T}}_{r_{t-1}}$ is diagonal. As a result, the normal likelihood is evaluated with non-diagonal matrices, which does not respect the physical assumptions verified in the measured environments. In such a case, the posterior statistics of the different channels cannot be factorized, even if their likelihoods are separable. This issue can be illustrated through the generative process for data following a bivariate t-distribution (Kotz and Nadarajah, 2006):

$$\mathbf{x}_t = \frac{\sqrt{\nu}}{s_t}\mathbf{y}_t + \boldsymbol{\mu}, \tag{16}$$

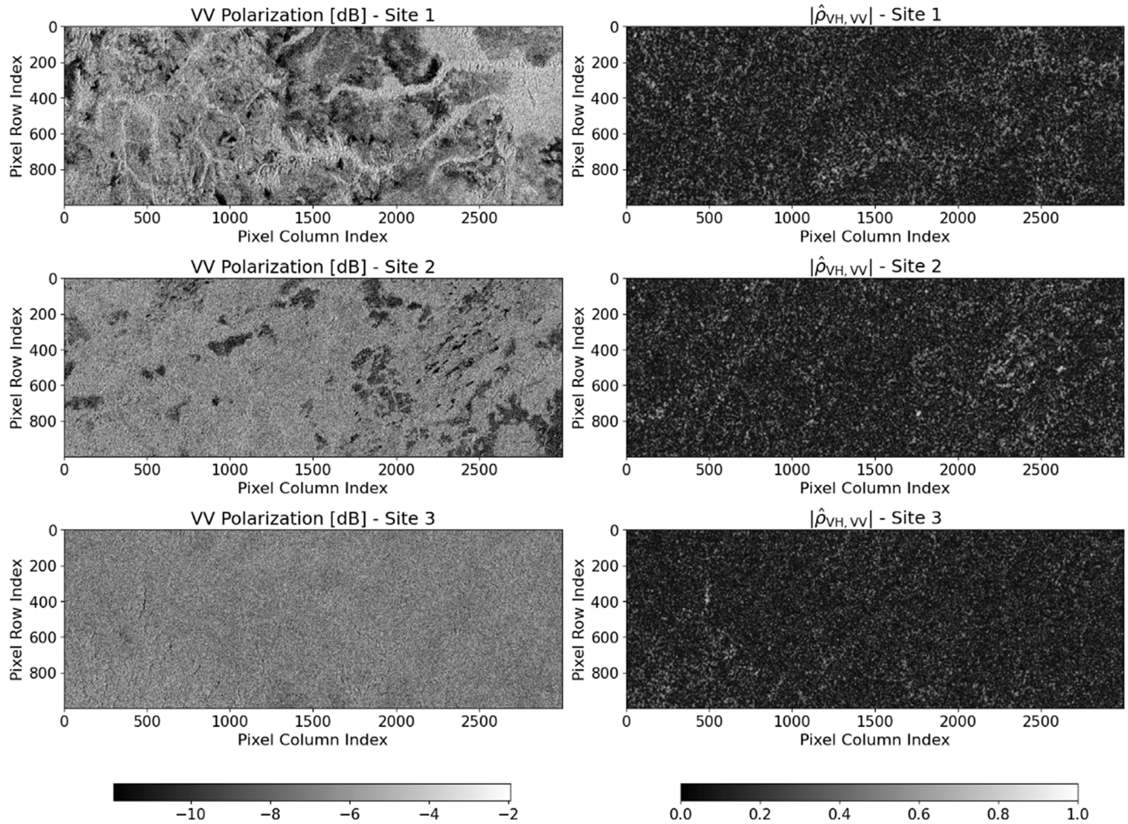

Fig. 5. ζ^0_{VV} of three sites in the Cerrado biome (1000 × 3000 pixels) (left). Corresponding correlation maps computed using a boxcar filter of size $N = 11$ (right).

where $\mathbf{y}_t \sim \mathcal{N}(\mathbf{0}, \mathbf{C})$ and $s_t^2 \sim \chi^2_\nu$. The definition in (16) shows that all components of $\mathbf{y}_t$ are similarly affected by the factor s_t, which induces mutual dependence between the dimensions of $\mathbf{x}_t$, even when $\mathbf{C}$ is diagonal.

Factorized BOCD. Another approach is to leverage reflection symmetry to factorize the data likelihood as:

$$p_{\boldsymbol{\Theta}}(\mathbf{x}_t) = \prod_{i=1}^{2} p_{\theta_i}(x_{i,t}), \tag{17}$$

where $\boldsymbol{\Theta}$ represents the set of parameters $\{\theta_i\}_{i=1}^2$. The posterior predictive distribution between two changepoints is given by:

$$p\left(\mathbf{x}_t|\mathbf{X}_{t-1}^{(r_{t-1})}\right) = \prod_{i=1}^{2} \int p(x_{i,t}|\theta_i)\, \pi_{\boldsymbol{\eta}_i}(\boldsymbol{\theta}_i|\mathbf{x}_{i,t-1}^{(r_{t-1})})\, d\boldsymbol{\theta}_i. \tag{18}$$

In the present case of two uncorrelated, normally distributed sources, the posterior predictive distribution can be expressed in the general form:

$$p\left(\mathbf{x}|\mathbf{X}_m\right) = \prod_{i=1}^{2} f_i(x_i; \boldsymbol{\eta}_i(m)), \tag{19}$$

with $\mathbf{X}_m = (\mathbf{x}_0, \dots, \mathbf{x}_m)$, $\boldsymbol{\eta}_i(m) = (\mu_{i,m}, \alpha_{i,m}, \kappa_{i,m}, \beta_{i,m})$, and:

$$f_i(x_{i,t}; \boldsymbol{\eta}_i(m)) = t_{2\alpha_{i,m}}\left(x_{i,t}\middle|\mu_{i,m}, \frac{\beta_{i,m}(\kappa_{i,m}+1)}{\alpha_{i,m}\kappa_{i,m}}\right). \tag{20}$$

The individual parameters in (20) can be updated as:

$$\begin{aligned}
\mu_{i,m} &= \frac{\kappa_{i,0}\mu_{i,0} + m\overline{x}_i}{\kappa_{i,0} + m} \\
\alpha_{i,m} &= \alpha_{i,0} + \frac{m}{2} \\
\kappa_{i,m} &= \kappa_{i,0} + m \\
\beta_{i,m} &= \beta_{i,0} + \frac{1}{2}\sum_{i=0}^{m}(x_i - \overline{x}_i)^2 + \frac{m\kappa_{i,0}}{\kappa_{i,0}+m}\frac{(\overline{x} - \mu_{i,0})^2}{2},
\end{aligned} \tag{21}$$

with $\boldsymbol{\eta}_i(0) = \boldsymbol{\eta}_{i,0}$ and $\overline{x}_i = \sum_{i=0}^{m} x_i/(m+1)$. The polarimetric BOCD with factorized likelihoods is referred to as $f\,pol$-BOCD, and it reduces the complexity of generic posterior predictive processing to twice the cost of the univariate approach.

The factorization process previously introduced is equivalent to adjusting the underlying generative process of the standard t-distribution to better capture the properties of the data under analysis (Kotz and Nadarajah, 2006). In this study, Sentinel-1 polarimetric data are better represented by independent modulation factors, as follows:

$$\mathbf{x}_t = \begin{bmatrix} \frac{\sqrt{\nu}}{s_{VV_t}} & 0 \\ 0 & \frac{\sqrt{\nu}}{s_{VH_t}} \end{bmatrix} \mathbf{y}_t + \boldsymbol{\mu}, \tag{22}$$

which is equivalent to evaluating the summation in (15) within the space of diagonal covariance matrices.

4.2. Detection strategy and parameter setting

At time t, the most probable run length *a posteriori*, denoted as M_t, corresponds to the value of r_t that maximizes the posterior probability in (5) given the observations up to time t. In the absence of change, this run length increases linearly over time, following the relation $M_t = M_{t-1} + 1$. Conversely, the occurrence of a changepoint is indicated by a drop in the run length index, as M_t becomes smaller than M_{t-1}. The value to which it drops depends on the detection delay. Specifically, the change event occurs at time $t_c = t - M_t$ but is only detected M_t acquisitions later. To avoid false alarms due to random fluctuations in the time series, a threshold is applied: a change is detected if M_t decreases by more than a fixed margin ΔM, that is, when $M_t < M_{t-1} - \Delta M$, with ΔM a positive constant. ΔM should be interpreted as the length of the algorithm's initialization period, during which detections are not accounted for, rather than as a data-dependent detection threshold. Its role is solely to prevent early false alarms and it does not affect the detector's sensitivity once sufficient observations are available. As such, it is independent of acquisition characteristics (e.g., revisit time, noise level, or biome-specific variability) and only plays a role when the initialization period represents a non-negligible fraction of the observations, such as in short time series or when a change occurs at the very beginning of the observation window.

In the univariate BOCD algorithm, susceptibility to detecting forest loss events is adjusted by modifying key parameters such as the priors of the posterior predictive distribution (Bottani et al., 2025a). A similar approach can be applied to the polarimetric BOCD variants. It can be observed from (21) that, with a sufficiently large number of observations, μ and β converge to their respective sample estimates. Conversely, adjusting α and κ is the most effective way to influence susceptibility to changes. Smaller values of α or κ increase the sensitivity of BOCD, making the algorithm more prone to flagging changes. The following analysis uses $\Delta M = 10$ for all method variants and adopts the following prior configurations:

- $gpol$-BOCD and $dpol$-BOCD: $\boldsymbol{\mu}_0 = (x_{1,1}, x_{2,1})$, $\alpha_0 = 3$, $\kappa_0 = 0.01$, $\mathbf{T}_0 = \mathrm{diag}(1,1)$.
- $fpol$-BOCD (applied separately to each univariate t-distribution): $\mu_{i,0} = x_{i,1}$, $\alpha_{i,0} = 0.001$, $\kappa_{i,0} = 0.01$, $\beta_{i,0} = 0.01$.

4.3. Analysis of detection timeliness

Verifying a method's temporal accuracy of forest loss detections is a complex task. Precise performance evaluation requires knowledge of the actual deforestation date for each parcel, which is often unavailable. The temporal performance of the considered methods in detecting forest loss over the reference datasets is assessed using the 'DTIMGANT' and 'DTIMGDEP' attributes provided by MapBiomas Alerta. Specifically, 'DTIMGANT' represents the last date a parcel was observed as vegetated, so any detection prior to this date is considered a false alarm. In contrast, 'DTIMGDEP' is the first date a parcel was observed as disturbed, indicating that deforestation occurred before this date. The detection dates identified by the considered methods are first compared to 'DTIMGANT' to ensure plausibility, and then compared to 'DTIMGDEP' to assess the detection delay relative to MapBiomas Alerta. To ensure a fair comparison, the methods are evaluated over a set of polygons detected by each method in at least a specified percentage, i.e., T_{poly} in (1), of their area. Additionally, at the polygon level, the detection delay described in Section 4.2 is computed as the median of individual pixel delays to minimize the impact of outliers.

5. Results

This section presents forest loss detection results obtained using $fpol$-BOCD (19) and other BOCD variants. Specifically, the single-polarization methods, VH-BOCD and VV-BOCD, as well as the union, $VH \cup VV$, and intersection, $VH \cap VV$, of their results, are evaluated using the reference datasets derived from MapBiomas Alerta (Section 2.4). Additionally, the $gpol$-BOCD (Section 4.1.1) and $dpol$-BOCD (Section 4.1.3) variants are evaluated using the Cerrado reference dataset. In the Cerrado, the results are further compared with alerts from the optical-based GLAD-L system (Hansen et al., 2016), as well as the gross forest cover loss yearly dataset (Hansen et al., 2013) (accessed on: https://www.glad.umd.edu/). The latter is referred to as *Yearly Loss* and does not represent NRT information; instead, it provides a yearly assessment of forest cover loss, computed from Landsat imagery. In the Amazon, results are compared with alerts from the operational SAR-based method RADD (Reiche et al., 2021) (accessed on: https://www.wur.nl/).

5.1. Spatial analysis of deforestation detection results

Two examples of deforestation detection comparing $fpol$-BOCD to VH-BOCD and VV-BOCD, are shown in Figs. 6 and 7. Fig. 6 highlights the improvement in spatial accuracy achieved by incorporating both polarimetric channels within $fpol$-BOCD compared to single-polarization methods. In contrast, Fig. 7 demonstrates a case where VH-BOCD detected the change on 07/12/2020, while VV-BOCD identified it earlier, on 20/09/2020. In this instance, $fpol$-BOCD detected the deforestation event on 20/09/2020, effectively combining the superior spatial precision of VH with the faster detection capability of VV. For the interested reader, the full maps of forest loss detection in the Cerrado and Amazonia for 2020, obtained using $fpol$-BOCD on the reference datasets, are shown in Appendix.

Cerrado. The performance metrics of the evaluated methods are reported in Tables 2 and 3, for small- and large-scale clearings, respectively. Specifically, the F1-score is computed as $F_1 = 2ps/(p+s)$, where precision $p = TP/(TP+FP)$, and sensitivity $s = TP/(TP+FN)$. The results demonstrate the superior performance of $fpol$-BOCD in detecting small clearings, with improvements of 23% over VV-BOCD at T_{poly} =75%, 47% over GLAD-L, and 30% over *Yearly Loss*. Additionally, the joint processing of VV and VH time series within $fpol$-BOCD improves the detection performance of VH-BOCD by 9%. Both single-polarization BOCD methods outperform GLAD-L and *Yearly Loss* in terms of true positives. It should be noted that GLAD-L does not operate on savanna formations, which partly explains its limited performance, while *Yearly Loss* does not provide timely information.

The union of single-polarization BOCD results, $VH \cup VV$, yields a marginal improvement of 0.4% in true positive detections at $T_{poly} = 75\%$ compared to $fpol$-BOCD, but this comes at the cost of increased false alarms, which rise from 6.7% at $T_{poly} = 75\%$ to 34.9% at $T_{poly} = 10\%$ This behavior is well reflected in the F1-scores, where $fpol$-BOCD consistently achieves the best performance across all considered T_{poly} values. Furthermore, the intersection of single-polarization BOCD results, $VH \cap VV$, shows a tendency toward omission, with a decrease of 26% at $T_{poly} = 75\%$, despite its robustness to false alarms. All considered methods appear robust to false alarms at high T_{poly} values, with the exception of $VH \cup VV$. However, at low T_{poly}, a moderate increase in false alarm rates is observed for all methods. The union $VH \cup VV$ shows the highest false alarm rate, approximately 30% higher than the second-worst method *Yearly Loss*. This is followed by VH-BOCD and $fpol$-BOCD, VV-BOCD, and finally GLAD-L. The results obtained by $gpol$-BOCD and $dpol$-BOCD demonstrate improvements in true detections compared to single-polarization methods, highlighting the benefits of incorporating dual-polarization information. However, their performance remains below that of $fpol$-BOCD, which more effectively models the statistical decorrelation between polarization channel. Ultimately, $fpol$-BOCD allows the detection of additional disturbed areas in both the forest and savanna categories compared to using only the cross-polarized channel.

The results for large clearings exclude the intermediate methods $gpol$-BOCD and $dpol$-BOCD, as well as the optical datasets *Yearly Loss* and GLAD-L, since their performance is comparable to that observed for small-scale clearings. The outcomes reveal two major differences compared to the performance observed for small-scale clearings. First, the performance improvement of $fpol$-BOCD over VH-BOCD decreases from 9% at $T_{poly} = 75\%$ to 3.4% when considering larger disturbed areas. Second, the overall change detection performance of $fpol$-BOCD increases by approximately 17% at $T_{poly} = 75\%$ when detecting larger deforested areas.

Amazonia. The performance metrics of the evaluated methods are reported in Tables 4 and 5, for small- and large-scale clearings, respectively. Results over small clearings show that $fpol$-BOCD achieves a 34% increase in true positive detections compared to RADD at $T_{poly} = 75\%$. In contrast, only a marginal improvement of 0.4% at $T_{poly} = 75\%$ is

(a) ©Google Earth (b) VH-BOCD (c) VV-BOCD (d) $fpol$-BOCD

Fig. 6. Example (1) comparing detections by different BOCD methods. Central pixel location: (43.24722°W, 4.20829°S), area: 1.2 hectares.

(a) ©Google Earth (b) VH-BOCD (c) VV-BOCD (d) $fpol$-BOCD

Fig. 7. Example (2) comparing detections by different BOCD methods. Central pixel location: (45.40366°W, 19.96494°S), area: 1.5 hectares.

Table 2
Detection performance evaluated in the Cerrado using the small-clearings reference dataset (i.e., A_0). T_{poly} defined in (1).

T_{poly}	$fpol$-BOCD	$dpol$-BOCD	$gpol$-BOCD	VH-BOCD	VV-BOCD	$VH \cup VV$	$VH \cap VV$	Yearly Loss	GLAD-L
				True Positive (TP) [%]					
75%	**48.8**	46.2	44.6	**39.9**	26.1	**49.2**	22.9	18.9	1.2
50%	81.0	76.2	75.6	71.7	56.6	81.2	46.6	43.7	5.9
10%	97.1	96.4	96.1	95.9	91.2	97.0	89.0	75.2	28.2
				False Positive (FP) [%]					
75%	0	0	0	0	0	**6.7**	0	0	0.2
50%	0	0	0	0	0	13.5	0	0	0.2
10%	3.9	3.9	3.9	3.9	1.9	34.9	0.9	4.3	0.9
				F1-Score [%]					
75%	**65.6**	63.2	61.7	**57.1**	41.4	**65.4**	37.3	31.8	2.4
50%	89.5	86.5	86.1	83.5	72.3	88.2	63.6	60.8	11.2
10%	98.1	97.8	97.6	97.5	95.2	94.9	94.1	85.4	43.9
				Land Cover Distribution of True Positive Detections at $T_{poly} = 75\%$					
Forest	56.0	53.5	52.6	54.9	57.4	53.7	64.8	59.4	100
Savanna	44.0	46.5	47.4	45.1	42.6	46.3	35.2	40.6	0

Table 3
Detection performance evaluated in the Cerrado using the large-clearings reference dataset. $A_1 - A_3$ defined in Table 1. T_{poly} defined in (1). 'ALL' indicates performance over the entire dataset.

T_{poly}	$fpol$-BOCD				VH-BOCD				VV-BOCD				$VH \cup VV$				$VH \cap VV$			
	ALL	A_1	A_2	A_3	ALL	A_1	A_2	A_3	ALL	A_1	A_2	A_3	ALL	A_1	A_2	A_3	ALL	A_1	A_2	A_3
									True Positive (TP) [%]											
75%	**61.2**	61.9	57.0	65.9	**57.8**	56.1	52.5	66.7	44.8	39.7	46.4	50.0	**61.6**	61.9	57.5	66.7	39.2	41.8	34.1	47.0
50%	71.2	72.5	71.5	68.9	68.2	70.4	67.0	67.4	60.8	60.8	58.7	63.6	71.8	73.0	73.2	68.2	54.8	54.0	53.1	58.3
10%	91.2	91.0	91.0	91.7	90.6	90.5	85.7	90.9	80.2	82.5	76.0	82.6	90.4	89.9	90.5	90.9	73.8	76.7	72.6	71.2
									False Positive (FP) [%]											
75%	0	0	0	0	0	0	0	0	0	0	0	0	7.2	15.9	6.9	4.5	0	0	0	0
50%	0	0	0	0	0	0	0	0	0	0	0	0	17.6	29.5	23.6	10.4	0	0	0	0
10%	2.4	11.4	1.4	0	2.0	11.4	0	0	1.2	4.5	1.4	0	39.2	40.9	48.6	33.6	0.4	0	1.4	0
									F1-Score [%]											
75%	**75.9**	76.5	72.6	79.5	**73.3**	71.9	68.9	80.0	61.9	56.8	63.4	66.7	**74.6**	74.8	71.8	77.9	56.3	55.7	50.8	63.9
50%	83.2	84.0	83.4	81.6	81.1	82.6	80.3	80.5	75.6	75.7	73.9	77.8	79.5	81.2	80.1	76.3	70.8	70.1	69.3	73.9
10%	94.8	94.0	95.0	95.7	94.6	93.7	95.0	95.2	88.7	89.9	86.1	90.5	86.1	90.2	86.2	80.8	84.8	86.8	83.9	83.2
									Land Cover Distribution of True Positive Detections at $T_{poly} = 75\%$											
Forest	56.5	56.4	54.9	58.6	55.4	54.7	53.2	58.4	54.9	50.7	59.0	54.5	57.8	63.2	55.3	53.4	54.1	56.2	50.8	54.8
Savanna	43.5	43.6	45.1	41.4	44.6	45.3	46.8	41.6	45.1	49.3	41.0	45.5	42.2	36.8	44.7	46.6	45.9	43.8	49.2	45.2

Table 4
Detection performance evaluated in Amazonia using the small-clearings reference dataset (i.e., A_0). T_{poly} defined in (1).

T_{poly}	$fpol$-BOCD	VH-BOCD	VV-BOCD	$VH \cup VV$	$VH \cap VV$	RADD
True Positive (TP) [%]						
75%	**71.0**	**69.6**	54.3	**71.0**	36.7	**37.3**
50%	86.8	74.8	65.9	86.6	51.8	66.6
10%	97.7	92.8	86.6	97.3	82.9	88.3
False Positive (FP) [%]						
75%	0	0	0	**6.3**	0	0.2
50%	1.3	1.2	1.0	10.8	0.2	0.5
10%	5.5	4.2	4.0	24.1	0.7	5.5
F1-Score [%]						
75%	**83.1**	**82.1**	70.4	81.8	53.6	**54.3**
50%	92.6	90.5	81.2	90.4	68.2	79.9
10%	96.6	95.3	91.9	93.4	90.5	92.7

Table 5
Detection performance evaluated in Amazonia using the large-clearings reference dataset. $A_1 - A_3$ defined in Table 1. T_{poly} defined in (1). 'ALL' indicates performance over the entire dataset.

T_{poly}	$fpol$-BOCD				VH-BOCD				VV-BOCD				$VH \cup VV$				RADD			
	ALL	A_1	A_2	A_3	ALL	A_1	A_2	A_3	ALL	A_1	A_2	A_3	ALL	A_1	A_2	A_3	ALL	A_1	A_2	A_3
True Positive (TP) [%]																				
75%	**38.8**	40.1	37.6	36.5	**28.6**	32.2	24.3	23.8	24.2	25.8	22.5	22.2	**38.0**	39.8	36.4	34.9	**35.0**	37.9	31.8	31.7
50%	60.4	62.5	61.8	47.6	51.6	53.0	52.0	44.4	43.8	47.3	42.2	33.3	59.4	62.1	60.7	44.4	65.6	70.1	61.3	58.7
10%	90.8	95.1	93.1	66.7	86.2	90.2	87.9	65.1	83.0	86.4	86.1	60.3	90.2	94.7	92.5	65.1	91.6	92.4	92.5	85.7
False Positive (FP) [%]																				
75%	0	0	0	0	0	0	0	0	0	0	0	0	**7.6**	9.1	8.5	2.2	0	0	0	0
50%	0.4	0.9	0	0	0.4	0.9	0	0	0	0	0	0	10.8	15.5	9.6	4.3	0.8	0.9	1.1	0
10%	2.4	3.6	2.1	0	2.4	3.6	2.1	0	1.6	2.7	1.1	0	16.4	20.9	14.9	8.7	2.8	3.6	3.2	0
F1-Score [%]																				
75%	**55.9**	57.3	54.6	53.5	**44.5**	48.7	39.1	38.5	39.0	41.0	36.8	36.4	**53.6**	55.4	51.6	51.2	**51.9**	54.9	48.2	48.2
50%	75.2	76.7	76.4	64.5	68.0	69.1	68.4	61.5	60.9	64.3	59.3	50.0	72.0	73.7	73.2	60.2	79.0	82.2	75.7	74.0
10%	94.6	96.7	95.8	80.0	92.0	94.1	93.0	78.8	90.3	92.1	92.3	75.2	90.9	93.1	92.2	75.9	94.9	95.3	95.2	92.3

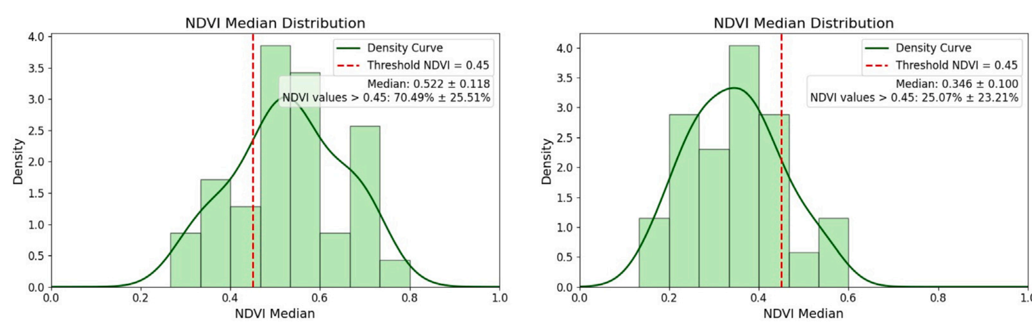

(a) Over polygons showing improved $fpol$-BOCD performance

(b) Over polygons showing similar $fpol$-BOCD and VH-BOCD performance

Fig. 8. Density curves of median NDVI values from Sentinel-2 imagery for polygons in Amazonia. The dashed red line marks the empirical threshold of 0.45.

observed over VH-BOCD. Similar to the trend observed in the Cerrado, the union of single-polarization alerts leads to a substantial increase in false alarms compared to $fpol$-BOCD, despite achieving comparable true positive detections. The intersection of single-polarization results yields poor detection performance, despite offering robustness against false alarms. The overall detection performance of $fpol$-BOCD for small clearings in Amazonia is 22% higher at T_{poly} = 75% compared to that for small clearings in the Cerrado.

Results for large-scale deforested areas in the Amazon highlight that processing VH and VV jointly with $fpol$-BOCD yields a 10% increase in true detections at T_{poly} = 75% compared to VH-BOCD. Similar conclusions to those reported previously apply to the union of single-polarization results (i.e., higher false alarms compared to $fpol$-BOCD despite comparable detections). The intersection of results yields unsatisfactory detection performance and has therefore been omitted from Table 5. For large clearings, $fpol$-BOCD achieves a 4% increase in true positive detections compared to RADD at T_{poly} = 75%, with comparable false alarm rates. The overall detection performance of $fpol$-BOCD for large clearings in Amazonia is 32% lower than that for small clearings at T_{poly} = 75%, indicating an inverse trend compared to the outcomes observed in the Cerrado.

5.1.1. Characteristics of polygons with improved detection

For the polygons in Amazonia where $fpol$-BOCD achieves improved detections over VH-BOCD at T_{poly} = 75%, the Normalized Difference Vegetation Index (NDVI) derived from Sentinel-2 multispectral imagery on the detection date identified by $fpol$-BOCD is analyzed and shown in Fig. 8. Results indicate that median NDVI values are generally higher

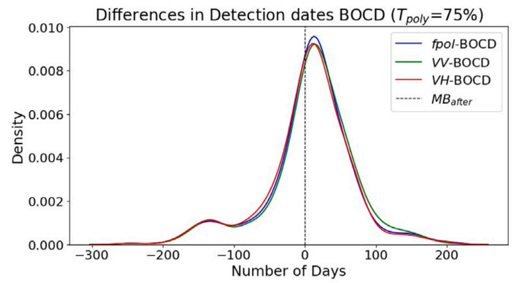

(a) $T_{poly} = 75\%$

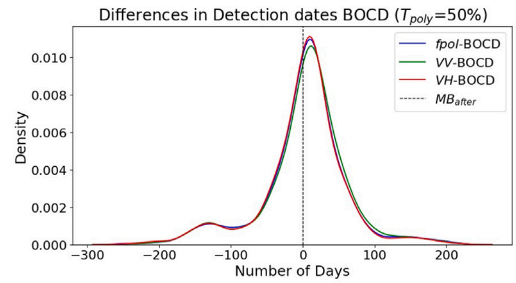

(b) $T_{poly} = 50\%$

Fig. 9. Density curves of detection date differences between BOCD methods compared to MapBiomas Alerta ($t_{MB_{after}}$).

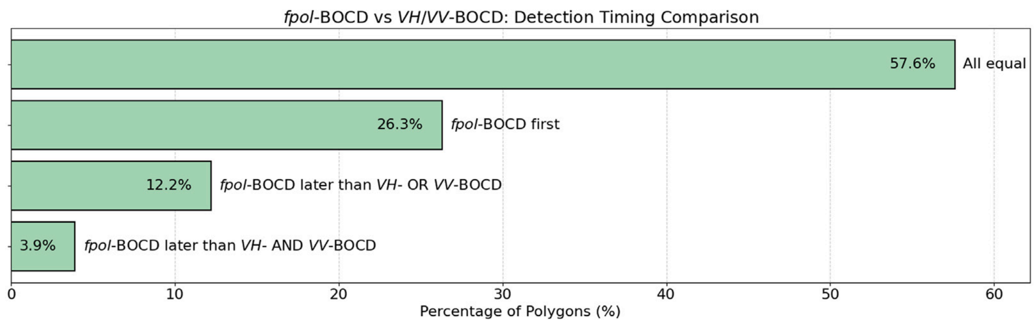

Fig. 10. Detection timing comparison between $fpol$-BOCD and VH/VV-BOCD.

than the empirical threshold of 0.45 in polygons where $fpol$-BOCD outperforms VH-BOCD (Fig. 8(a)), whereas the opposite pattern is observed in polygons where VH-BOCD performs comparably to $fpol$-BOCD (Fig. 8(b)). Visual examples of polygons where the polarimetric approach improves detection performance, or where its performance is comparable to that of the cross-polarization channel, are shown in Figs. A.13 and A.14 in Appendix.

A quantitative analysis of the empirical VV–VH correlation over the polygons before and after deforestation, performed by computing the coefficient $|\hat{\rho}|_{VH,VV}$ as described in Section 4.1.2, supports the factorization assumption underlying $fpol$-BOCD. Across the Amazon and Cerrado biomes, the estimated median correlation is $\hat{\mu} \approx 0.27$ with standard deviation $\hat{\sigma} \approx 0.16$, over both completely cleared polygons and polygons likely affected by residual vegetation

5.2. Temporal analysis of deforestation detection results

The density curves showing the differences in detection dates between BOCD methods and 'DTIMGDEP', i.e., MB_{after}, are shown in Fig. 9. Comparisons with GLAD-L and RADD are omitted, since similar results are reported in a previous study (Bottani et al., 2025a). The results show comparable detection delays across the BOCD methods, with a median delay of 3 acquisitions for all approaches.

Detection timing is further assessed for polygons commonly detected by all three methods in both Amazon and Cerrado biomes ($T_{poly} = 75\%$, 4437 polygons), with results shown in Fig. 10. The analysis demonstrates that in most cases all three methods detect changes simultaneously, in a substantial fraction of cases $fpol$-BOCD detects earlier than the single-polarization methods, and only in a minority of cases it detects later.

The monthly forest loss detection counts obtained by $fpol$-BOCD, categorized by land cover type, are presented in Fig. 11 for both the Cerrado and the Amazon. In the Cerrado (Fig. 11(a)), the results highlight that the peak in forest loss detections occurs in August, during the dry season. However, a significant number of detections, especially within the forest category, are recorded toward the end of the year (October to December), which typically coincides with the rainy season. In the Amazon (Fig. 11(b)), deforestation peaks in August, with significant activity also observed in July and September. A gradual decrease in deforestation activity is observed toward the end of the year, with the exception of slightly higher counts in December than in November.

6. Discussion

6.1. Contribution of polarimetry in forest loss monitoring

The results on the detection of small and large deforested areas in both the Cerrado and Amazon biomes (Section 5.1) highlight two major points regarding the contribution of polarimetry. First, the joint use of VH and VV polarization channels within $fpol$-BOCD improves detection performance for small clearings in the Cerrado by 9% at $T_{poly} = 75\%$ (Table 2), and for large clearings in the Amazon by 10% at the same threshold (Table 5), compared to VH-BOCD. Second, the overall $fpol$-BOCD performance is 22% lower for small clearings compared to large clearings in the Cerrado, and 32% lower for large clearings compared to small clearings in the Amazon.

These facts are likely explained by the distinct deforestation practices observed in the Cerrado and the Amazon. In the Cerrado, large-scale clearings are often associated with industrial soy cultivation (Rausch et al., 2019), where land is cleared systematically and efficiently, leaving behind uniform expanses of bare, dry soil. In such cases, VH polarization is particularly effective, as it excels at detecting reductions in volume scattering. Conversely, subsistence farming and smallholder agriculture — typically responsible for smaller clearings — often involve artisanal clearing methods, which may leave behind patches of residual vegetation (Rasmussen et al., 2016). Over small deforested areas, VV polarization showed a significant contribution, likely due to its sensitivity to ground scattering, which may be advantageous for detecting non-uniform areas. Conversely, in the Amazon, the primary method of forest clearing is "slash-and-burn" agriculture (Bezerra et al., 2024), which involves cutting down the forest and

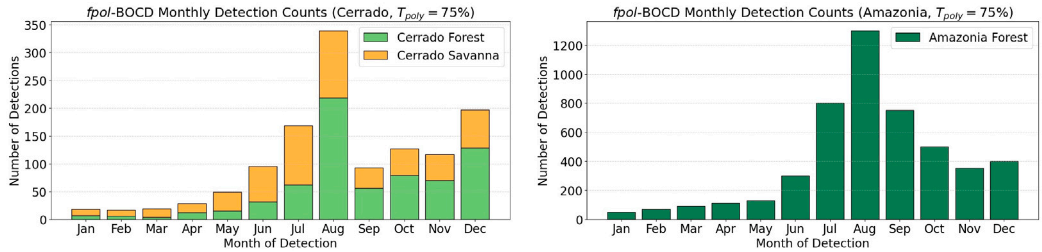

(a) Cerrado (b) Amazonia

Fig. 11. Monthly forest loss detection counts for 2020 (T_{poly}=75%), obtained using $fpol$-BOCD, differentiated by land cover type.

subsequently burning the biomass. The cutting and burning stages are typically separated, as the fallen wood is allowed to dry due to its high moisture content. This method is particularly common in larger clearings, given the challenges associated with removing dense and extensive forest biomass (Mataveli et al., 2021), resulting in prolonged periods of residual vegetation remaining on the ground.

Overall, the results show that incorporating VV polarization within $fpol$-BOCD enhances deforestation detection in parcels likely corresponding to areas where residual biomass remains on the ground rather than being completely cleared, as indicated by the higher median NDVI in polygons where $fpol$-BOCD improves detection compared to VH-BOCD (Fig. 8(a)). In contrast, over parcels that are fully cleared and thus exhibit lower NDVI values (Fig. 8(b)), VH polarization generally outperforms VV and is often sufficient for accurate detection. Overall detection performance is, however, higher when deforested parcels are fully cleared and homogeneous.

6.2. Spatial performance comparison of deforestation detection

Cerrado. The detection results in Table 2 highlight the superior performance of $fpol$-BOCD compared to optical-based methods, i.e., GLAD-L and *Yearly Loss*, in detecting small clearings. Furthermore, $fpol$-BOCD achieves a consistent and meaningful gain of 9% in true positives over VH-BOCD at T_{poly} = 75%, while maintaining robustness to false alarms. This improvement is particularly notable given the lower contrast typically observed in the VV channel, suggesting that the added robustness stems from leveraging an additional, uncorrelated measurement dimension. This is further supported by the unsatisfactory results obtained when combining single-polarization BOCD detections: $VH \cup VV$ suffers from the aggregation of false alarms from the different processing chains, while $VH \cap VV$ yields low true positive rates. Similar conclusions about merging individual polarization results apply when detecting large clearings (Table 3). However, for large-scale disturbances, the improvement of $fpol$-BOCD over VH-BOCD is only marginal.

Further analysis reveals that the joint processing of VH and VV data enhances deforestation detection in both forest and savanna areas (Tables 2 and 3). Interestingly, despite savannas having more reference polygons, forested areas show the highest number of detections. This can be explained by the fact that forest loss monitoring using C-band data relies heavily on the contrast between intact vegetation and deforestation. Forested areas typically exhibit the most significant backscatter drops after clearing, as shown in Fig. 2. Savannas follow with a notable backscatter reduction post-clearing, which is often sufficient to detect deforestation events. The joint usage of VH and VV channels within $fpol$-BOCD enables the exploitation of the optimal contrast between intact vegetation and deforestation, which may occur in either channel depending on specific conditions, thus improving detection capabilities.

Amazonia. The results in Table 4 show that $fpol$-BOCD outperforms RADD by 34% at T_{poly} = 75% for detecting small clearings, while providing only marginal improvements over VH-BOCD. The low performance of RADD in this context is attributed to the use of speckle filtering, which significantly reduces the spatial resolution of Sentinel-1 data and can therefore hinder the detection of small deforested areas. For large clearings (Table 5), the improvement of $fpol$-BOCD over RADD decreases to 4% at the same threshold, while its improvement over VH-BOCD increases to 10%. In particular, when detecting larger disturbances, spatial resolution becomes less critical.

6.3. Temporal performance of deforestation detection

The comparison of detection timeliness across methods and against MapBiomas Alerta reveals generally consistent performance among the BOCD-based methods, as the vast majority of reference polygons, i.e., 57.6%, experience change detection on the same date (Figs. 9 and 10). However, in a minority of cases, the timeliness of $fpol$-BOCD can be constrained by the slower detection among the single-polarization VH and VV methods. This is considered acceptable given the improved spatial detection performance of $fpol$-BOCD and the fact that it achieves earlier detection in 26.3% of cases.

Forest loss activity peaks in August, consistently across both studied biomes (Fig. 11). Notably, the timing of the peak aligns with expectations, as the dry season is typically associated with increased deforestation efforts (RAD2023, 2024). However, fewer detections occur at the beginning of the dry season (April to June) compared to later in the year (September to December), which typically marks the end of the dry season and the onset of heavy rains. In the Cerrado (Fig. 11(a)), this pattern is particularly evident in the forest category. Notably, a significant number of $fpol$-BOCD detections in the Cerrado are located at lower latitudes near the boundary with the Amazon (Fig. A.12(a)) and belong to the forest category (Fig. 1). Furthermore, in the Amazon, many $fpol$-BOCD detections are located along the southwestern frontier with Bolivia and Peru (Fig. A.12(b)). Recent studies have reported increased climate pressures in both the eastern Cerrado–Amazon transition zone (Marengo et al., 2022) and the southwestern Amazon (Leite-Filho et al., 2019), where ongoing deforestation has contributed to a lengthening of the dry season. This trend is linked to reduced precipitation, which prolongs dry conditions and may further encourage deforestation. The higher number of detections during the wet season likely reflects this dynamic, as the extended dry season enables deforestation activities even in months typically characterized by higher rainfall.

6.4. Seasonality and detection of progressive changes

The results obtained in the Cerrado biome demonstrate that $fpol$-BOCD is robust against seasonal fluctuations, as it is specifically designed to detect rapid and persistent changes in SAR backscatter time series. Gradual or subtle changes — such as slow canopy thinning or progressive forest degradation with marginal inter-acquisition backscatter differences — exhibit patterns similar to seasonal fluctuations and may not generate sufficient statistical evidence to trigger a changepoint, potentially remaining undetected. However, gradual changes that are cumulative and persistent, for example fire-induced forest degradation over multiple acquisitions, can still be identified once the deviation from the original backscatter distribution becomes statistically significant and sustained (Bottani et al., 2025b). This property enables the method to maintain robustness against natural variability while capturing meaningful progressive changes.

6.5. Future research

The findings of this study highlight the advantages of jointly using dual-polarization Sentinel-1 data to detect deforestation across heterogeneous areas, particularly in cases where residual vegetation remains after clearing activities. Future work will explore how to further improve detection performance by integrating additional complementary data sources. One promising direction is to incorporate time series from both ascending and descending Sentinel-1 orbits, to further enhance detection accuracy and spatial coverage. Additionally, adapting the framework to process optical imagery, such as that from Sentinel-2, could offer significant benefits. Sentinel-2 data provides higher spatial resolution, is easier to interpret, and offers a clearer deforestation signature, which could complement radar-based information. Furthermore, its spatial alignment with Sentinel-1 is advantageous for multi-source fusion. However, the challenge posed by cloud coverage, especially over tropical regions, limits the availability of consistent Sentinel-2 acquisitions. Another avenue worth exploring is the integration of lower-frequency SAR data, such as L- or P-band, which can penetrate deeper into the canopy and are less sensitive to surface saturation. Incorporating such data could further enhance detection performance in areas with residual vegetation, where C-band backscatter alone may still retain a significant volume scattering component. To address these challenges, future work will focus on adapting the framework to process multiple, differently distributed, and asynchronous sources of information—combining radar data from Sentinel-1 with optical imagery from Sentinel-2, as well as lower-frequency data from NISAR and BIOMASS. This will require handling missing data and effectively integrating the datasets to maximize detection capabilities while accounting for their inherent differences. Leveraging the strengths of all information sources is expected to further enhance the accuracy and reliability of deforestation monitoring in operational environments.

7. Conclusion

This work explored the use of dual-polarization Sentinel-1 time series for forest loss detection across mixed land cover types. The analysis revealed that while VH polarization generally offers higher contrast between intact vegetation and deforested areas, making it more suitable for forest loss monitoring, VV polarization may be more effective in specific contexts. For instance, VV polarization may be advantageous for detecting biomass remnants after clearing. Building on these insights, this study introduced $fpol$-BOCD, an unsupervised Bayesian polarimetric change detection method with NRT capabilities. The $fpol$-BOCD approach processes dual-polarization Sentinel-1 acquisitions without introducing additional computational complexity beyond the single-polarization methods previously investigated in Bottani et al. (2025a).

The method's deforestation detection capabilities were evaluated using two reference datasets provided by MapBiomas Alerta in the Cerrado and Amazon biomes in 2020: a first dataset containing small clearings, and a second dataset comprising larger clearings selected through a stratified sampling approach. The detection results were compared with outputs from single-polarization BOCD methods, VH-BOCD and VV-BOCD, and combinations of single-polarization detections, $VH \cup VV$ and $VH \cap VV$. An additional comparison was conducted against the operational optical-based GLAD-L alerts in the Cerrado and the operational SAR-based RADD alerts in the Amazon.

Detection results showed that jointly processing dual-polarization data within $fpol$-BOCD improved the detection of small-scale clearings in the Cerrado and large-scale clearings in the Amazon by approximately 10% compared to VH-BOCD. In contrast, improvements were marginal for large clearings in the Cerrado and small ones in the Amazon. These outcomes were attributed to the distinct deforestation practices typical of the two biomes. In the Cerrado, large-scale clearings — often associated with mechanized soy cultivation — are executed systematically, leaving behind uniformly bare soil. In such conditions, VH polarization is particularly effective due to the sharp reduction in volume scattering, rendering VV polarization comparatively less informative. In contrast, smallholder agriculture and subsistence farming typically involve artisanal clearing methods, which often leave substantial residual vegetation or debris. Under these less uniform conditions, VV polarization is considered to contribute more significantly, complementing VH in the detection of subtle structural changes. In the Amazon, an opposite pattern takes place: large clearings typically involve cutting down the forest, allowing it to dry, and then burning the biomass, as removing extensive vegetation from dense rainforest areas is logistically challenging. In terms of detection timeliness, $fpol$-BOCD matched single-polarization methods and outperformed both the union and intersection of single-polarization results. Furthermore, $VH \cup VV$ suffers from a high rate of false alarms, whereas $VH \cap VV$ suffers from a low rate of true detections. It also surpassed GLAD-L in the Cerrado and RADD in the Amazon (for small clearings), benefiting from its higher spatial resolution.

A temporal analysis of deforestation detections revealed that the peak in forest loss occurred during the dry season, which aligns with expected patterns of increased deforestation activities. However, an unexpected concentration of detections during the early months of the wet season suggested that changes in seasonal patterns, such as the lengthening of the dry season, may be influencing deforestation dynamics. This observation warrants further investigation into how shifting seasonal patterns may alter deforestation behavior and how monitoring methods can be adapted to these changes. Overall, the findings highlighted the potential of $fpol$-BOCD to enhance deforestation detection, particularly in areas where clearing practices leave behind residual vegetation that introduce textural complexity in the radar signals.

CRediT authorship contribution statement

Marta Bottani: Writing – review & editing, Writing – original draft, Visualization, Validation, Software, Methodology, Investigation, Formal analysis, Data curation, Conceptualization. **Laurent Ferro-Famil:** Writing – review & editing, Writing – original draft, Supervision, Methodology, Formal analysis, Conceptualization. **Thuy Le Toan:** Writing – review & editing, Supervision, Conceptualization. **Juan Doblas Prieto:** Writing – review & editing, Supervision, Software. **Stéphane Mermoz:** Writing – review & editing, Supervision. **Thierry Koleck:** Supervision, Resources.

Declaration of competing interest

The authors declare that they have no known competing financial interests or personal relationships that could have appeared to influence the work reported in this paper.

Acknowledgments

Marta Bottani's research was funded by the Centre National d'Études Spatiales (CNES) and ISAE Supaero, with the work conducted at the TéSA and CESBIO laboratories in Toulouse, France. This study also benefited from partial funding through the EUR TESS grant (N° ANR-18-EURE-0018) under the Programme des Investissements d'Avenir, as well as additional support from ISAE Supaero and GdR IASIS mobility grants.

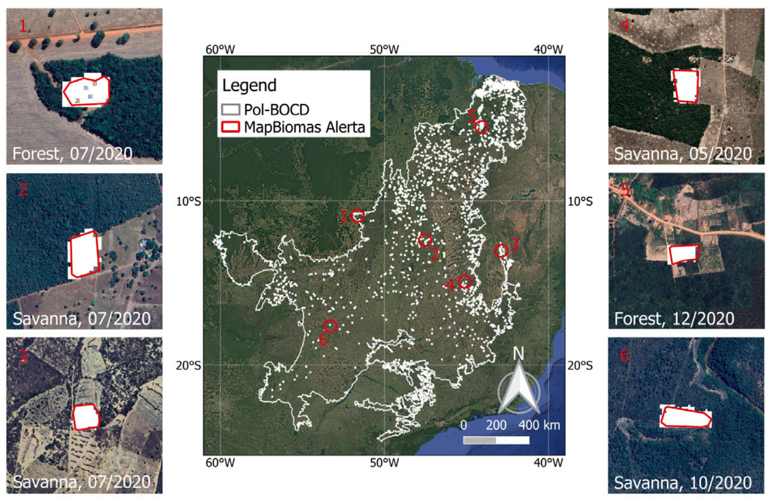

(a) Cerrado

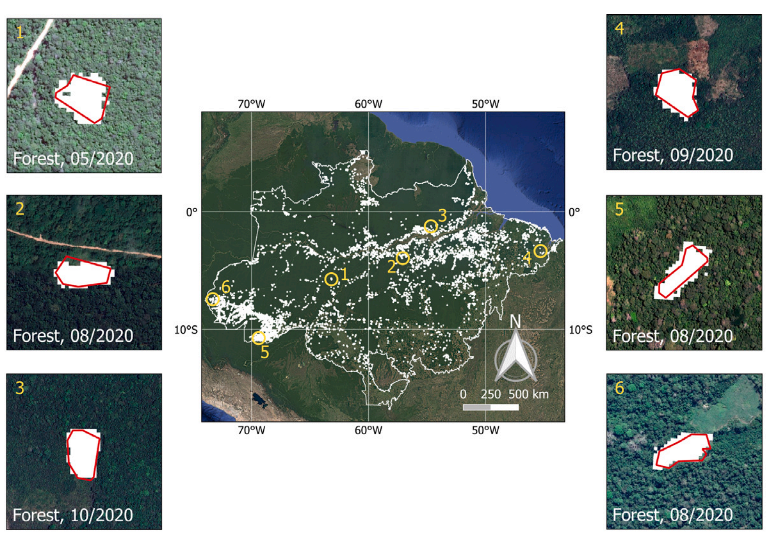

(b) Amazonia

Fig. A.12. Forest loss detection map from $fpol$-BOCD in 2020, with examples of reference polygons from the validation dataset in red. All polygons are cleared for agricultural purposes. Optical background image sourced from Google Earth (©2025 Google).

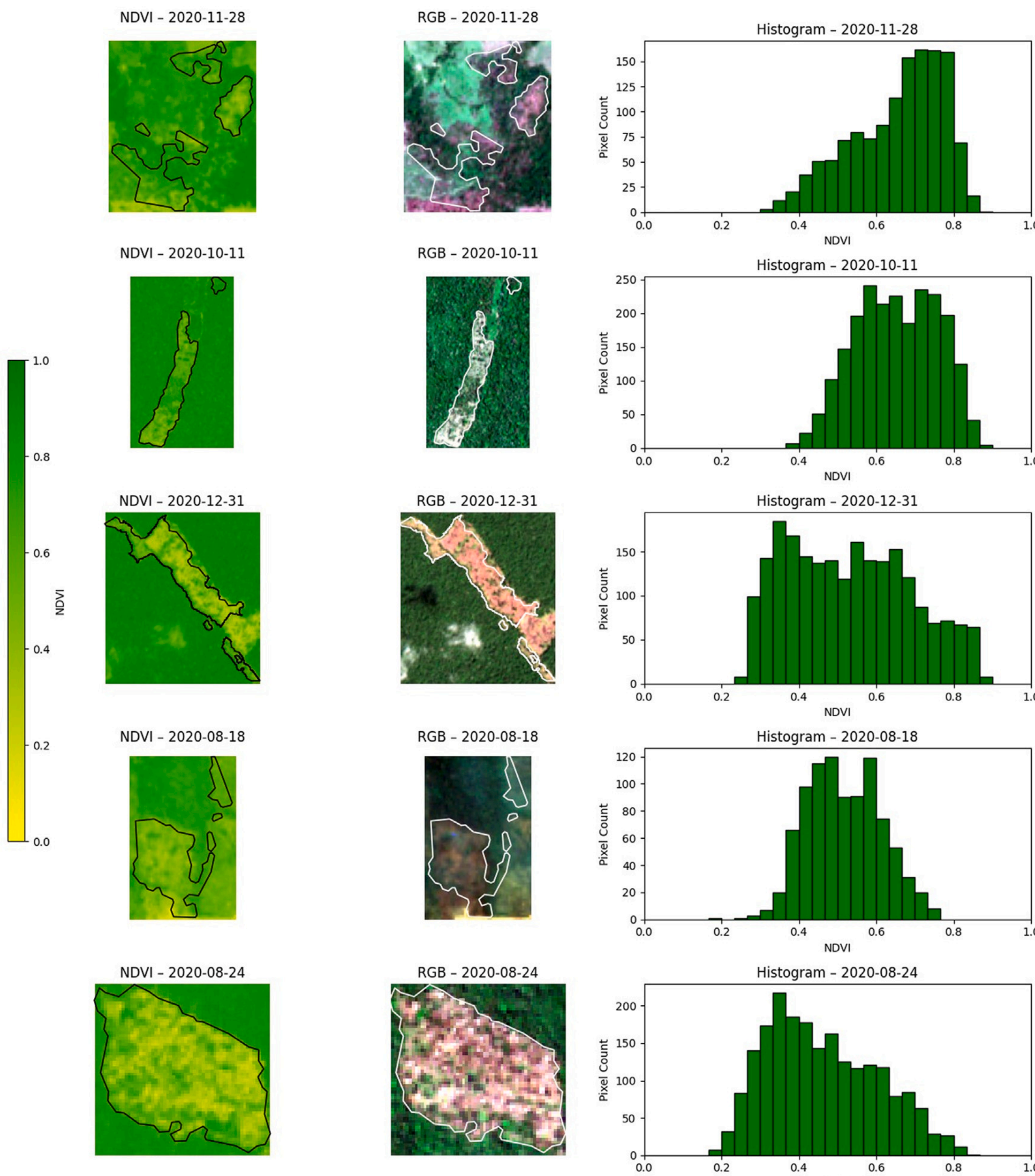

Fig. A.13. Examples of polygons where $fpol$-BOCD improves detection vs. VH-BOCD. Column 1: NDVI computed at the $fpol$-BOCD detection date. Column 2: RGB composite. Column 3: Histogram of NDVI values within the polygon.

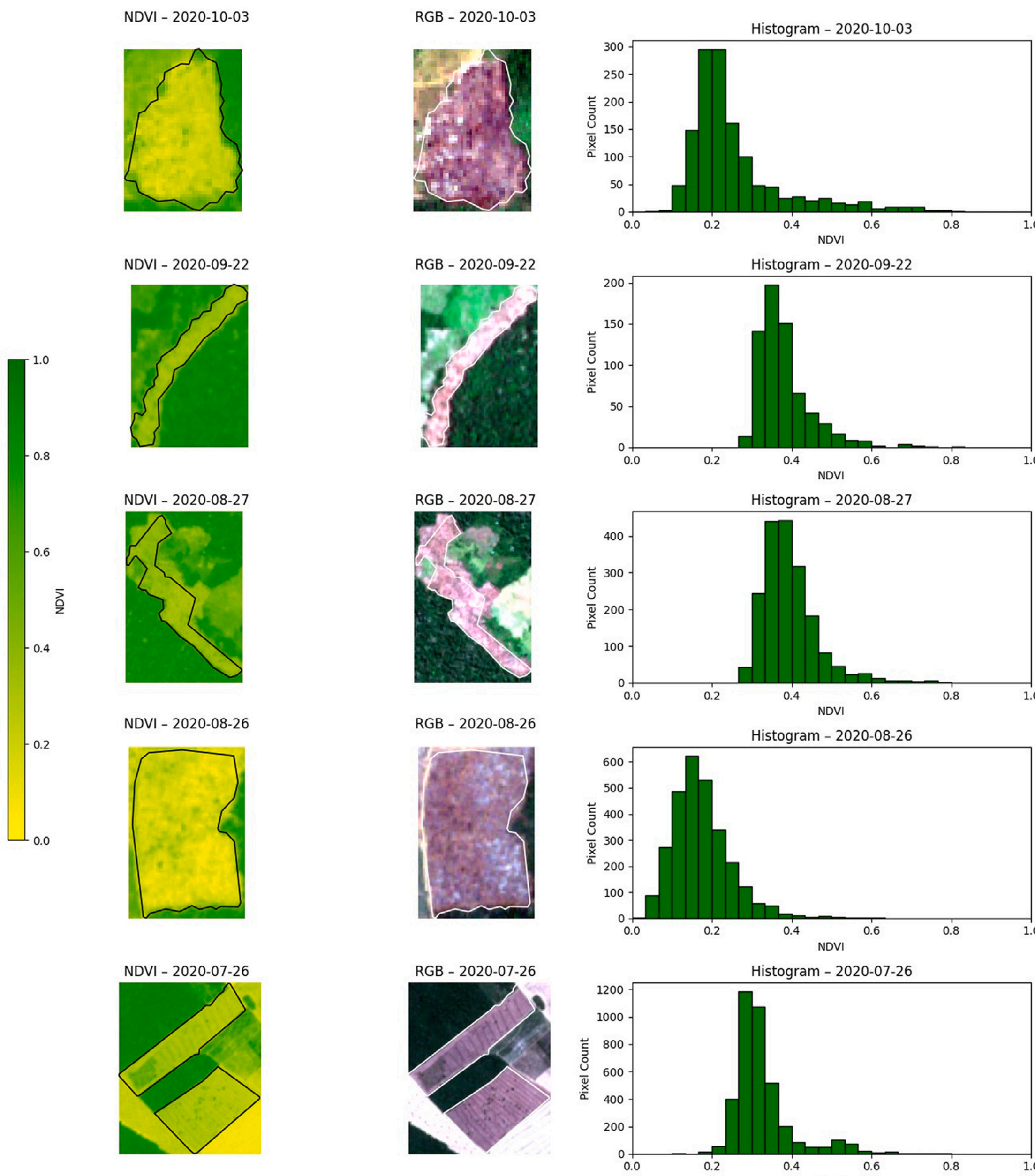

Fig. A.14. Examples of polygons where $fpol$-BOCD and VH-BOCD show comparable detections. Column 1: NDVI computed at the $fpol$-BOCD detection date. Column 2: RGB composite. Column 3: Histogram of NDVI values within the polygon.

Appendix. Supplementary results

See Figs. A.12–A.14.

References

Abdo, R., Ferro-Famil, L., Boutet, F., Allain-Bailhache, S., 2021. Analysis of the double-bounce interaction between a random volume and an underlying ground, using a controlled high-resolution PolTomoSAR experiment. Remote. Sens. 13 (4), http://dx.doi.org/10.3390/rs13040636.

Acker, A., 2021. Amazon Development. Oxford University Press, http://dx.doi.org/10.1093/acrefore/9780199366439.013.837.

Adams, R.P., MacKay, D.J., 2007. Bayesian online changepoint detection. http://dx.doi.org/10.48550/arXiv.0710.3742.

Arii, M., van Zyl, J.J., Kim, Y., 2010. A general characterization for polarimetric scattering from vegetation canopies. IEEE Trans. Geosci. Remote Sens. 48 (9), 3349–3357. http://dx.doi.org/10.1109/TGRS.2010.2046331.

Asner, G.P., Knapp, D., Broadbent, E., Oliveira, P., Keller, M., Silva, J., 2005. Selective logging in the Brazilian amazon. Science 310, 480–482. http://dx.doi.org/10.1126/science.1118051.

Azevedo, T., Rosa, M.R., Shimbo, J.Z., de Oliveira, M.G., 2021. Relatório Anual do Desmatamento no Brasil 2020. Technical Report, MapBiomas, São Paulo, Brasil, URL: http://alerta.mapbiomas.org.

Ballère, M., Bouvet, A., Mermoz, S., Toan, T.L., Koleck, T., Bedeau, C., André, M., Forestier, E., Frison, P.-L., Lardeux, C., 2021. SAR data for tropical forest disturbance alerts in french guiana: Benefit over optical imagery. Remote Sens. Environ. 252, 112159. http://dx.doi.org/10.1016/j.rse.2020.112159.

Bezerra, J.S., Arroyo-Rodríguez, V., Arasa-Gisbert, R., Meave, J.A., 2024. Multiscale effects of slash-and-burn agriculture across the tropics: Implications for the sustainability of an ancestral agroecosystem. Sustainability 16 (22), http://dx.doi.org/10.3390/su16229994.

Bottani, M., Ferro-Famil, L., Doblas Prieto, J., Mermoz, S., Bouvet, A., Koleck, T., Le Toan, T., 2025a. Novel unsupervised Bayesian method for near real-time forest loss detection using sentinel-1 SAR time series: Assessment over sampled deforestation events in Amazonia and the Cerrado. Remote Sens. Environ. 331, 115037. http://dx.doi.org/10.1016/j.rse.2025.115037.

Bottani, M., Ferro-Famil, L., René, P.-C., Polidori, L., 2025b. Continuous monitoring of fire-induced forest loss using sentinel-1 SAR time series and a Bayesian method: A case study in paragominas, Brazil. Remote. Sens. 17, 2822. http://dx.doi.org/10.3390/rs17162822.

Bourgeau-Chavez, L.L., Leblon, B., Charbonneau, F., Buckley, J.R., 2013. Evaluation of polarimetric radarsat-2 SAR data for development of soil moisture retrieval algorithms over a chronosequence of black spruce boreal forests. Remote Sens. Environ. 132, 71–85. http://dx.doi.org/10.1016/j.rse.2013.01.006.

Bouvet, A., et al., 2018. Use of the SAR shadowing effect for deforestation detection with sentinel-1 time series. Remote. Sens. 10, 1250. http://dx.doi.org/10.3390/rs10081250.

Carstairs, H., Mitchard, E.T.A., McNicol, I., Aquino, C., Chezeaux, E., Ebanega, M.O., Dikongo, A.M., Disney, M., 2022. Sentinel-1 shadows used to quantify canopy loss from selective logging in gabon. Remote. Sens. 14 (17), http://dx.doi.org/10.3390/rs14174233.

Cloude, S., Pottier, E., 1996. A review of target decomposition theorems in radar polarimetry. IEEE Trans. Geosci. Remote Sens. 34 (2), 498–518. http://dx.doi.org/10.1109/36.485127.

Cloude, S., Pottier, E., 1997. An entropy based classification scheme for land applications of polarimetric SAR. IEEE Trans. Geosci. Remote Sens. 35 (1), 68–78. http://dx.doi.org/10.1109/36.551935.

De Andrade Aragão, R., Lima Bastos, G.M., Burns, G.L., Ross, H., 2022. To clear or not to clear: Unpacking soy farmers' decision-making on deforestation in Brazil's cerrado. Front. Sustain. Food Syst. 6, http://dx.doi.org/10.3389/fsufs.2022.942207.

Doblas, J., Reis, M.S., Belluzzo, A.P., Quadros, C.B., Moraes, D.R.V., Almeida, C.A., Maurano, L.E.P., Carvalho, A.F.A., Sant'Anna, S.J.S., Shimabukuro, Y.E., 2022. DETER-R: An operational near-real time tropical forest disturbance warning system based on sentinel-1 time series analysis. Remote. Sens. 14 (15), http://dx.doi.org/10.3390/rs14153658.

Doblas, J., et al., 2020. Optimizing near real-time detection of deforestation on tropical rainforests using sentinel-1 data. Remote. Sens. 12, 3922. http://dx.doi.org/10.3390/rs12233922.

Durden, S., van Zyl, J., Zebker, H., 1989. Modeling and observation of the radar polarization signature of forested areas. IEEE Trans. Geosci. Remote Sens. 27 (3), 290–301. http://dx.doi.org/10.1109/36.17670.

El-Hajj, M., Baghdadi, N.N., Zribi, M., Bazzi, H., 2017. Synergic use of sentinel-1 and sentinel-2 images for operational soil moisture mapping at high spatial resolution over agricultural areas. Remote. Sens. 9, 1292. http://dx.doi.org/10.3390/rs9121292.

FAO, 2020. Global Forest Resources Assessment 2020: Main Report. Technical Report, FAO, Rome.

Ferro-Famil, L., Pottier, E., 2014. Chapter 21 - radar polarimetry basics and selected earth remote sensing applications. In: Sidiropoulos, N.D., Gini, F., Chellappa, R., Theodoridis, S. (Eds.), Academic Press Library in Signal Processing: Volume 2. In: Academic Press Library in Signal Processing, vol. 2, Elsevier, pp. 1119–1244. http://dx.doi.org/10.1016/B978-0-12-396500-4.00021-1.

Ferro-Famil, L., Pottier, E., Jong-Sen, L., 2001. Unsupervised classification of multifrequency and fully polarimetric SAR images based on the H/A/Alpha-Wishart classifier. IEEE Trans. Geosci. Remote Sens. 39 (11), 2332–2342. http://dx.doi.org/10.1109/36.964969.

Fink, D., 1997. A Compendium of Conjugate Priors. Technical Report, Montana State Univeristy, URL: https://www.johndcook.com/CompendiumOfConjugatePriors.pdf.

Freeman, A., Durden, S., 1998. A three-component scattering model for polarimetric SAR data. IEEE Trans. Geosci. Remote Sens. 36 (3), 963–973. http://dx.doi.org/10.1109/36.673687.

Furtado, L.F., Silva, T.S.F., Novo, E., 2016. Dual-season and full-polarimetric C band SAR assessment for vegetation mapping in the Amazon várzea wetlands. Remote Sens. Environ. 174, 212–222. http://dx.doi.org/10.1016/j.rse.2015.12.013.

Hansen, M.C., Krylov, A., Tyukavina, A., Potapov, P.V., Turubanova, S., Zutta, B., Ifo, S., Margono, B., Stolle, F., Moore, R., 2016. Humid tropical forest disturbance alerts using landsat data. Environ. Res. Lett. 11, 034008. http://dx.doi.org/10.1088/1748-9326/11/3/034008.

Hansen, M.C., Potapov, P.V., Moore, R.M., Hancher, M., Turubanova, S., Tyukavina, A., Thau, D., Stehman, S., Goetz, S., Loveland, T.R., Kommareddy, A., Egorov, A.V., Chini, L.P., Justice, C.O., Townshend, J.R., 2013. High-resolution global maps of 21st-century forest cover change. Science 342, 850–853. http://dx.doi.org/10.1126/science.1244693.

Hoekman, D., Quiñones, M., 2000. Land cover type and biomass classification using AirSAR data for evaluation of monitoring scenarios in the Colombian amazon. IEEE Trans. Geosci. Remote Sens. 38, 685–696. http://dx.doi.org/10.1109/36.841998.

Hoekman, D., et al., 2020. Wide-area near-real-time monitoring of tropical forest degradation and deforestation using sentinel-1. Remote. Sens. 12, 3263. http://dx.doi.org/10.3390/rs12193263.

Huynen, J., 1970. Phenomenological Theory of Radar Targets (Ph.D. thesis). Rotterdam, The Netherlands.

Imhoff, M.L., 1995. Radar backscatter and biomass saturation: ramifications for global biomass inventory. IEEE Trans. Geosci. Remote Sens. 33, 511–518. http://dx.doi.org/10.1109/TGRS.1995.8746034.

Jiao, X., et al., 2011. The sensitivity of RADARSAT-2 polarimetric SAR data to corn and soybean leaf area index. Can. J. Remote Sens. 37, 69–81. http://dx.doi.org/10.5589/m11-023.

Joughin, I.R., Winebrenner, D.P., Percival, D.B., 1994. Probability density functions for multilook polarimetric signatures. IEEE Trans. Geosci. Remote Sens. 32, 562–574. http://dx.doi.org/10.1109/36.297975.

Kalamandeen, M., Gloor, M., Mitchard, E., Quincey, D., Ziv, G., Spracklen, D., Spracklen, B., Adami, M., Aragão, L., Galbraith, D., 2018. Pervasive rise of small-scale deforestation in amazonia. Sci. Rep. 8, http://dx.doi.org/10.1038/s41598-018-19358-2.

Karam, M., Fung, A., Lang, R., Chauhan, N., 1992. A microwave scattering model for layered vegetation. IEEE Trans. Geosci. Remote Sens. 30, 767–784. http://dx.doi.org/10.1109/36.158872.

Kotz, S., Nadarajah, S., 2006. Multivariate T-distributions and their applications. 101, http://dx.doi.org/10.1017/CBO9780511550683,

Le Toan, T., 2014. A P-band SAR for global forest biomass measurement: The BIOMASS mission. In: 2014 XXXIth URSI General Assembly and Scientific Symposium. URSI GASS, http://dx.doi.org/10.1109/URSIGASS.2014.6929692.

Lee, J., Pottier, E., 2009. Polarimetric Radar Imaging : From Basics to Applications. CRC Press, http://dx.doi.org/10.1201/9781420054989, Taylor & Francis Editor.

Leite-Filho, A., Pontes, V., Costa, M., 2019. Effects of deforestation on the onset of the rainy season and the duration of dry spells in southern amazonia. J. Geophys. Res.: Atmospheres 124, 5268–5281. http://dx.doi.org/10.1029/2018JD029537.

Lopez-Sanchez, J.M., Vicente-Guijalba, F., Ballester-Berman, J.D., Cloude, S.R., 2014. Polarimetric response of rice fields at C-band: Analysis and phenology retrieval. IEEE Trans. Geosci. Remote Sens. 52, 2977–2993. http://dx.doi.org/10.1109/TGRS.2013.2268319.

Magagi, R., et al., 2022. Potential of L-and C-bands polarimetric SAR data for monitoring soil moisture over forested sites. Remote. Sens. 14, 5317. http://dx.doi.org/10.3390/rs14215317.

Marengo, J.A., Jimenez, J.C., Espinoza, J.C., Cunha, A.P., Aragão, L.E.O., 2022. Increased climate pressure on the agricultural frontier in the eastern amazonia-cerrado transition zone. Sci. Rep. 12, 457. http://dx.doi.org/10.1038/s41598-021-04241-4.

Mataveli, G.A.V., de Oliveira, G., Seixas, H.T., Pereira, G., Stark, S.C., Gatti, L.V., Basso, L.S., Tejada, G., Cassol, H.L.G., Anderson, L.O., Aragão, L.E.O.C., 2021. Relationship between biomass burning emissions and deforestation in amazonia over the last two decades. Forests 12 (9), http://dx.doi.org/10.3390/f12091217.

Mermoz, S., et al., 2021. Continuous detection of forest loss in Vietnam, laos, and cambodia using sentinel-1 data. Remote. Sens. 13, 4877. http://dx.doi.org/10.3390/rs13234877.

Miranda, J., Börner, J.J., Kalkuhl, M., Soares-Filho, B.S., 2019. Land speculation and conservation policy leakage in Brazil. Environ. Res. Lett. 14, http://dx.doi.org/10.1088/1748-9326/ab003a.

Mullissa, A., Reiche, J., Herold, M., 2023. Deep learning and automatic reference label harvesting for sentinel-1 SAR-based rapid tropical dry forest disturbance mapping. Remote Sens. Environ. 298, 113799. http://dx.doi.org/10.1016/j.rse.2023.113799.

Mullissa, A., Saatchi, S., Silva, R., Erickson, T., Provost, N., Osborn, F., Ashary, A., Moon, V., Melling, D., 2024. LUCA: A sentinel-1 SAR-based global forest land use change alert. Remote. Sens. 16, 2151. http://dx.doi.org/10.3390/rs16122151.

Murphy, K.P., 2007. Conjugate Bayesian Analysis of the Gaussian Distribution. Technical Report, The University of British Columbia, URL: https://www.cs.ubc.ca/~murphyk/Papers/bayesGauss.pdf.

Neumann, M., Ferro-Famil, L., Reigber, A., 2010. Estimation of forest structure, ground, and canopy layer characteristics from multibaseline polarimetric interferometric SAR data. IEEE Trans. Geosci. Remote Sens. 48 (3), 1086–1104. http://dx.doi.org/10.1109/TGRS.2009.2031101.

Nghiem, S.V., et al., 1992. Symmetry properties in polarimetric remote sensing. Radio Sci. 27 (05), 693–711. http://dx.doi.org/10.1029/92RS01230.

Nunes, S., Barlow, J., Gardner, T., Siqueira, J., Sales, M., Souza, Jr., C., 2014. A 22 year assessment of deforestation and restoration in riparian forests in the eastern Brazilian amazon. Environ. Conserv. 1, 1–11. http://dx.doi.org/10.1017/S0376892914000356.

Papathanassiou, K.P., Cloude, S.R., Pardini, M., Quiñones, M.J., Hoekman, D., Ferro-Famil, L., 2021. Forest applications. In: Hajnsek, I., Desnos, Y.-L. (Eds.), Polarimetric Synthetic Aperture Radar: Principles and Application. Springer, pp. 59–117.

Persson, H., Mukhopadhyay, R., Huuva, I., Fransson, J., 2022. Comparison of boreal biomass estimations using C- and X-Band polsar. In: IGARSS 2022 - 2022 IEEE International Geoscience and Remote Sensing Symposium. pp. 5555–5558. http://dx.doi.org/10.1109/IGARSS46834.2022.9884506.

Picard, G., Toan, T.L., Quegan, S., Caraglio, Y., Castel, T., 2004. Radiative transfer modeling of cross-polarized backscatter from a pine forest using the discrete ordinate and eigenvalue method. IEEE Trans. Geosci. Remote Sens. 42, 1720–1730. http://dx.doi.org/10.1109/TGRS.2004.831229.

Pinheiro, T.F., Pinto, J.F.S.K.C., de Carvalho, M.A., Sestini, M.F., Pettinati, D.R., Santos, J.O., dos Santos, S.B., Soler, L.D.S., Scheide, A.D., Messias, C.G., Almeida, C.A., Amaral, S., Moreira, T.A., Dousseau, S.L., Moraes, D.D.C., Costa, J.D.S., Nisimura, T.D.M., 2024. Uncovering patterns: Data mining the deforestation frontier in Brazilian cerrado. Int. Arch. Photogramm. Remote. Sens. Spat. Inf. Sci. XLVIII-3-2024, 401–406. http://dx.doi.org/10.5194/isprs-archives-XLVIII-3-2024-401-2024.

RAD2023, 2024. RAD 2023 : Annual Deforestation Report of Brazil 2023. Technical Report, São Paulo, Brazil, http://dx.doi.org/10.1088/1748-9326/ac5193.

Rasmussen, L., Jung, S., Brites, A., Watkins, C., Agrawal, A., 2016. Understanding smallholders' intended deforestation behavior in the Brazilian cerrado following environmental registry. Environ. Res. Lett. 12, http://dx.doi.org/10.1088/1748-9326/aa7ee5.

Ratter, J.A., Ribeiro, J.F., Bridgewater, S.G.M., 1997. The Brazilian cerrado vegetation and threats to its biodiversity. Ann. Botany 80, 223–230. http://dx.doi.org/10.1006/anbo.1997.0469.

Rausch, L., Gibbs, H., Schelly, I., Brandão Junior, A., Morton, D., Carneiro Filho, A., Strassburg, B., Nathalie, F., Noojipady, P., Barreto, P., Meyer, D., 2019. Soy expansion in Brazil's cerrado. Conserv. Lett. 12, http://dx.doi.org/10.1111/conl.12671.

Reiche, J., Hamunyela, E., Verbesselt, J., Hoekman, D., Herold, M., 2018a. Improving near-real time deforestation monitoring in tropical dry forests by combining dense sentinel-1 time series with landsat and ALOS-2 PALSAR-2. Remote Sens. Environ. 204, 147–161. http://dx.doi.org/10.1016/j.rse.2017.10.034.

Reiche, J., Mullissa, A., Slagter, B., Gou, Y., Tsendbazar, N.-E., Odongo-Braun, C., Vollrath, A., Weisse, M.J., Stolle, F., Pickens, A., Donchyts, G., Clinton, N., Gorelick, N., Herold, M., 2021. Forest disturbance alerts for the congo basin using sentinel-1. Environ. Res. Lett. 16 (2), 024005. http://dx.doi.org/10.1088/1748-9326/abd0a8.

Reiche, J., Richard, L., Mitchell, A.L., J. Verbesselt, D.H.H., Haarpaintner, J., Kellndorfer, J.M., Rosenqvist, A., Lehmann, E.A., Woodcock, C.E., Seifert, F.M., Herold, M., 2016. Combining satellite data for better tropical forest monitoring. Nat. Clim. Chang. 6, http://dx.doi.org/10.1038/nclimate2919.

Reiche, J., et al., 2018b. Characterizing tropical forest cover loss using dense sentinel-1 data and active fire alerts. Remote. Sens. 10, 777. http://dx.doi.org/10.3390/rs10050777.

Robb, R., Cochran, G., 1963. Sampling techniques. In: Proceedings of the Edinburgh Mathematical Society, second ed. John Wiley & Sons, 102532. http://dx.doi.org/10.1017/S0013091500025724.

Rosenqvist, A., Killough, B., 2018. A Layman's Interpretation Guide to L-band and C-band Synthetic Aperture Radar Data, v2.0. Technical Report, CEOS.

Shimabukuro, Y., Santos, J., Formaggio, A., Duarte, V., Rudorff, B., 2016. The Brazilian amazon monitoring program: PRODES and DETER projects. ISBN: 9780429086465, pp. 153–169. http://dx.doi.org/10.1201/b13040-9.

Skriver, H., 2012. Crop classification by multitemporal C- and L-band single- and dual-polarization and fully polarimetric SAR. IEEE Trans. Geosci. Remote Sens. 50, 2138–2149. http://dx.doi.org/10.1109/TGRS.2011.2172994.

Touzi, R., Lopes, A., Bruniquel, J., Vachon, P., 1999. Coherence estimation for SAR imagery. IEEE Trans. Geosci. Remote Sens. 37, 135–149. http://dx.doi.org/10.1109/36.739146.

Van Zyl, J., 1989. Unsupervised classification of scattering behavior using radar polarimetry data. IEEE Trans. Geosci. Remote Sens. 27 (1), 36–45. http://dx.doi.org/10.1109/36.20273.

Van Zyl, J., Kim, Y., 2011. Synthetic Aperture Radar Polarimetry. John Wiley & Sons, http://dx.doi.org/10.1002/9781118116104.

Veloso, A., et al., 2017. Understanding the temporal behavior of crops using sentinel-1 and sentinel-2-like data for agricultural applications. Remote Sens. Environ. 199, 415–426. http://dx.doi.org/10.1016/j.rse.2017.07.015.

Verbesselt, J., Zeileis, A., Herold, M., 2012. Near real-time disturbance detection using satellite image time series. Remote Sens. Environ. 123, 98–108. http://dx.doi.org/10.1016/j.rse.2012.02.022.

Veríssimo, A., Barreto, P., Mattos, M., Tarifa, R., Uhl, C., 1992. Logging impacts and prospects for sustainable forest management in an old amazonian frontier: The case of paragominas. Forest Ecol. Manag. 55, 169–199. http://dx.doi.org/10.1016/0378-1127(92)90099-U.

Ygorra, B., Frappart, F., Wigneron, J.-P., Moisy, C., Catry, T., Baup, F., Hamunyela, E., Riazanoff, S., 2021. Monitoring loss of tropical forest cover from sentinel-1 time-series: A cusum-based approach. Int. J. Appl. Earth Obs. Geoinf. 103, 102532. http://dx.doi.org/10.1016/j.jag.2021.102532.